

Supplementary Information for

Topological-insulating grain boundary networks for high-performance Fe₂VAl thermoelectrics

Fabian Garmroudi^{1,2,*}, Illia Serhiienko², Michael Parzer¹, Sanyukta Ghosh³, Pawel Ziolkowski³, Hieu Duy Nguyen⁴, Cédric Bourges^{2,5}, Yuya Hattori², Alexander Riss¹, Sebastian Steyrer¹, Gerda Rogl⁶, Peter Rogl⁶, Erhard Schafner⁷, Naoyuki Kawamoto⁴, Eckhard Müller^{3,8}, Johannes de Boor^{3,9,*}, Ernst Bauer¹, Takao Mori^{2,10,*}

¹Institute of Solid State Physics, TU Wien, 1040 Vienna, Austria

²International Center for Materials Nanoarchitectonics (WPI-MANA), National Institute for Materials Science (NIMS), Tsukuba, Japan

³Institute of Materials Research, German Aerospace Center (DLR), D-51147 Cologne, Germany

⁴Center for Basic Research on Materials (CBRM), NIMS, Tsukuba, Japan

⁵International Center for Young Scientists, National Institute for Materials Science (NIMS), Tsukuba, Japan

⁶Institute of Materials Chemistry, University of Vienna, 1090 Vienna, Austria

⁷Faculty of Physics, University of Vienna, 1090 Vienna, Austria

⁸Institute of Inorganic and Analytical Chemistry, Justus Liebig University Giessen, D-35392 Giessen, Germany

⁹University of Duisburg-Essen, Faculty of Engineering, Institute of Technology for Nanostructures (NST) and CENIDE, D-47057 Duisburg, Germany

¹⁰Graduate School of Pure and Applied Sciences, University of Tsukuba, Tsukuba, Japan

Contents

1	Materials and Methods	3	2
1.1	Synthesis of starting materials and composites.	3	3
1.2	Structural characterization.	3	4
1.3	High-temperature thermoelectric transport measurements.	4	5
1.4	Low-temperature thermoelectric transport measurements.	4	6
2	Electronic band structure model and estimation of bipolar thermal conductivity	5	7
2.1	Temperature-dependent electronic transport in the single-parabolic-band approximation	5	9
2.2	Multi-band and multi-carrier electronic transport	6	11
2.3	Modelling temperature-dependent transport in Fe ₂ V _{0.95} Ta _{0.1} Al _{0.95}	7	12

*Correspondence to: f.garmroudi@gmx.at,
Johannes.deBoor@dlr.de, mori.takao@nims.go.jp

13	3 Two-channel magneto-transport model	8
14	4 Grain refinement via high-pressure torsion	9
15	4.1 Attempts of reproducing high zT in $\text{Fe}_2\text{V}_{0.98}\text{Ta}_{0.1}\text{Al}_{0.92}$	9
16	4.2 Investigation of HPT processing of $\text{Fe}_2\text{V}_{0.95}\text{Ta}_{0.05}\text{Al}_{0.9}\text{Si}_{0.1}$ and other optimized	
17	full-Heusler systems	10
18	5 Additional micro- and nanostructure analyses	10
19	5.1 TEM investigation near the Heusler–Bi–Sb grain boundary	10
20	5.2 TEM investigation of a Heusler grain	11
21	6 Phonon band structures and densities of states	11
22	7 Isotropy of thermal transport	12
23	8 Supplementary Figures	14
24	8.1 HPT-deformed $\text{Fe}_2\text{V}_{0.98}\text{Ta}_{0.1}\text{Al}_{0.92}$: a comparison to literature	14
25	8.2 Effect of HPT on electronic transport in $\text{Fe}_2\text{V}_{0.95}\text{Ta}_{0.05}\text{Al}_{0.9}\text{Si}_{0.1}$	15
26	8.3 Effect of HPT processing for different Heusler samples	16
27	8.4 Additional microstructure investigation of $\text{Fe}_2\text{V}_{0.95}\text{Ta}_{0.1}\text{Al}_{0.95}$	17
28	8.5 Focused ion beam preparation of FVAB50 composite near a Heusler– $\text{Bi}_{1-x}\text{Sb}_x$	
29	grain boundary	18
30	8.6 Additional TEM investigation of a FIB-fabricated sample near the Heusler–	
31	$\text{Bi}_{1-x}\text{Sb}_x$ grain boundary	19
32	8.7 Additional high-resolution TEM of Heusler grains in FVAB50	20
33	8.8 EDX spectroscopy of nanoscale precipitates	21
34	8.9 Additional EDX analysis of two-phase microstructures	22
35	8.10 Additional SEM analysis of FVABX composites	23
36	8.11 Quantitative analysis of Bi/Sb concentrations in FVABX composites	24
37	8.12 X-ray powder diffraction patterns	25
38	8.13 Comparison of the temperature-dependent Seebeck coefficient of polycrystalline	
39	$\text{Bi}_{0.9}\text{Sb}_{0.1}$ with literature	26
40	8.14 Constructing an effective band structure model for $\text{Fe}_2\text{V}_{0.95}\text{Ta}_{0.1}\text{Al}_{0.95}$	27
41	8.15 Temperature-dependent Seebeck modelling of $\text{Bi}_{0.9}\text{Sb}_{0.1}$ and $\text{Fe}_2\text{V}_{0.95}\text{Ta}_{0.1}\text{Al}_{0.95}$	
42	starting materials	28
43	8.16 Effective medium theory predictions of dimensionless figure of merit	29
44	8.17 Additional magneto-transport data of FVAB50	30
45	8.18 Anomalous Hall effect of non-magnetic FVAB50 compared to other magnetic	
46	materials	31
47	8.19 Consistency check of temperature-dependent electrical resistivity	32
48	8.20 Phonon dispersion and density of states mismatch	33
49	8.21 Comparison of thermal conductivity in different directions of the sample . .	34

1. Materials and Methods

1.1. Synthesis of starting materials and composites.

Bulk elements of high purity (Fe 99.99%, V 99.93%, Ta 99.95%, Al 99.999%, Bi 99.999%, Sb 99.999%) were stoichiometrically weighed and polycrystalline ingots of the starting materials ($\text{Fe}_2\text{V}_{0.95}\text{Ta}_{0.1}\text{Al}_{0.95}$ and $\text{Bi}_{0.9}\text{Sb}_{0.1}$) were synthesized by high-frequency induction melting under Ar atmosphere. The as-cast ingots were manually crushed and ground using a tungsten carbide pestle and mortar. The resulting powders from the individual starting materials were then mixed in various volume ratios. The volume percentage of $\text{Bi}_{0.9}\text{Sb}_{0.1}$ powder added was adjusted and calculated based on the theoretical densities of the respective starting materials. After the powders were thoroughly mixed, the mixture was filled into a graphite die and sintered at a temperature of 1373 K, which is about 80% of the melting point of the full-Heusler phase and about 800 K higher than the melting point of $\text{Bi}_{0.9}\text{Sb}_{0.1}$. Consequently, excess liquid was expelled during the sintering process. Additionally, we observed that the liquid-phase sintering lead to a significant decrease in the sintering temperature of the Heusler material by up to almost 200 K when $\text{Bi}_{0.9}\text{Sb}_{0.1}$ powder was added as compared to when only $\text{Fe}_2\text{V}_{0.95}\text{Ta}_{0.1}\text{Al}_{0.95}$ powder was sintered. Nonetheless, to ensure consistent and comparable processing conditions for the samples studied in this work, all specimen were sintered using exactly the same synthesis conditions, i.e., a compaction pressure of 50 MPa, a maximum temperature of 1373 K and a holding time of 15 min. No additional heat treatment has been applied to the samples after the stintering process.

1.2. Structural characterization.

The microstructure and elemental composition of the sintered samples were investigated using scanning electron microscopy in both secondary electron (SE) and backscattered electron (BSE) modes, complemented by energy-dispersive X-ray spectroscopy (EDX). These analyses were performed on an ultra-high-resolution field emission SEM (HRSEM SU8230, Hitachi, Japan), equipped with an X-Max^N EDS detector (Horiba, Japan). For HRSEM observations, the samples were mounted in electroconductive epoxy and polished meticulously. EDX analysis utilized an acceleration voltage of 25 kV, gathering 10×10^6 counts per EDX map and 1×10^6 counts for point analysis.

To investigate the interface between the Fe_2VAl matrix and the $\text{Bi}_{0.9}\text{Sb}_{0.1}$ secondary phase at the nanoscale, the sample was prepared using a conventional focused ion beam (FIB) technique. A thin section was extracted from the targeted area (blue region in Figure S5), attached to an Omnigrid, and thinned to approximately 90 nm for electron transparency, as illustrated in Figure S5. Additionally, the FVAB50 sample was crushed into fine particles, dispersed in ethanol, and deposited on a grid to investigate the sample surface. Transmission electron microscopy (TEM) bright-field and lattice images were acquired using a JEOL JEM-3100FEF (JEOL, Japan) microscope operating at 300 kV, which was also equipped with an EDS detector for detailed elemental mapping.

The X-ray powder diffraction measurements were conducted at the Institute of Solid State Physics, TU Wien, using an in-house diffractometer (AERIS by PANalytical). These measurements utilized standard Cu K- α radiation, with data collected in the Bragg-Brentano

geometry over the angular range $20^\circ < 2\theta < 100^\circ$. Rietveld refinements on the obtained powder patterns were performed using the program PowderCell.

1.3. High-temperature thermoelectric transport measurements.

Thermal transport. The thermal conductivity measurements at high temperatures were performed in N_2 atmosphere directly on the sintered pellets, in the direction parallel to the pressing (compaction) direction during sintering with a commercially available setup (LFA 467 by NETZSCH). The instrument makes use of a conventional laser flash method for the diffusivity D and a differential scanning calorimeter for determining the specific heat c_p . The density of the sample d_m was determined via Archimedes principle and the thermal conductivity was calculated from $\kappa = D c_p d_m$.

Electronic transport. After the thermal conductivity measurements, the samples were cut into strips with $\approx 2 - 3$ mm in width and $\approx 8 - 10$ mm in length using a high-speed aluminum oxide cutting wheel. The bar-shaped samples were then mounted in a commercial setup (ZEM3 by ADVANCE RIKO) and the electrical resistivity and Seebeck coefficient were measured as a function of temperature. For the best sample, the measurement was repeated to confirm reproducible and stable results.

1.4. Low-temperature thermoelectric transport measurements.

Low-temperature measurements provide valuable insights into lower-energy excited states and states near the Fermi energy. This is especially significant for samples with narrow energy gaps, such as Fe_2VAl -based full-Heusler and binary $Bi_{1-x}Sb_x$ systems, where the Seebeck coefficient often peaks below or near room temperature. Furthermore, when modeling temperature-dependent data (using a parabolic band model for example), it is crucial that the experimental data span a wide temperature range. The thermoelectric characterization at low temperatures was carried out at TU Wien (Austria) on the same rectangular bar-shaped sample pieces that were used for the high-temperature measurements at NIMS (Japan).

Electrical resistivity. The temperature-dependent electrical resistivity was measured in a home-built bath cryostat at TU Wien, Austria. The sample was contacted in a four-probe geometry with thin gold wires using a spot-welding device. The sample was then mounted on a sample puck using GE Varnish as an adhesive and the sample probe was directly inserted into the cryostat. The measurement is performed continuously every time the temperature changes by about 1 K.

Seebeck coefficient. The temperature-dependent Seebeck coefficient was also measured on the very same sample piece using a different home-built setup at TU Wien, Austria. Here two chromel-constantan thermocouples are contacted to both ends of the sample to pick up the temperature difference and voltages. Since it is difficult to solder directly on the sample surface, a bundle of thick copper wires was first spot-welded onto the sample surface to which the thermocouples were then soldered. The high thermal conductivity of copper and the fact that the thermocouples are soldered in very close proximity to the sample surface ensures that the cold finger effect can be minimized. Furthermore, two strain gauges with a resistance of $\approx 120 \Omega$ function as heaters and are fixed to the bottom of both sample ends via GE varnish. The two heaters allow for switching the temperature difference ("seesaw

heating”¹⁾ to cancel spurious voltage contributions. The measurement is carried out in an evacuated sample chamber where He exchange gas can be put inside to ensure a thermal coupling to the cryogen (liquid helium).

Thermal conductivity. The thermal conductivity at low temperatures was measured by making use of a steady-state method using a home-built sample probe with a flow cryostat. Here, a heater is attached to the top surface of the sample employing a thermally conductive epoxy resin (STYCAST 2850FT). Similar to the Seebeck coefficient measurements, two bundles of copper wires are first fixed to the sample to each of which a thermocouple is then soldered. The bottom of the sample is mounted on a copper heat sink and the measurement is carried out in high vacuum ($\approx 10^{-5}$ mbar).

2. Modelling temperature-dependent transport and estimating bipolar thermal conductivity

The temperature-dependent transport properties of the single-phase starting materials (putting aside the nanoscale Ta-rich precipitates in $\text{Fe}_2\text{V}_{0.95}\text{Ta}_{0.1}\text{Al}_{0.95}$) were modelled using the *SeeBand* code, which is a recently developed powerful fitting algorithm based on the Boltzmann transport theory and the parabolic band approximation⁴. In semiclassical Boltzmann theory and in the isotropical case of spherical Fermi surfaces, the generalized transport coefficients $L_\alpha(\mu, T)$ can be written as

$$L_\alpha(\mu, T) = e^2 \int_{-\infty}^{\infty} D(E) v^2(E) \tau(E) (E - \mu)^\alpha \left(-\frac{\partial f}{\partial E} \right) dE. \quad (1)$$

with e being the elementary charge and $D(E)$, $v(E)$ and $\tau(E)$ being the electronic density of states, group velocity and relaxation time, respectively. The electrical conductivity, the Seebeck coefficient and the electronic part of the thermal conductivity are, for instance, directly determined by the transport coefficients in Equation 1 via the following expressions

$$\sigma = L_0(\mu, T), \quad (2)$$

$$S = \frac{L_1(\mu, T)}{T L_0(\mu, T)}, \quad (3)$$

and

$$\kappa_e = \frac{L_0(\mu, T) L_2(\mu, T) - L_1(\mu, T)^2}{T L_0(\mu, T)}. \quad (4)$$

2.1. Temperature-dependent electronic transport in the single-parabolic-band approximation

For parabolic bands it follows that $D(E) \propto E^{1/2}$, $v^2(E) \propto E$ and $\tau(E) \propto E^{-1/2}$ (when acoustic phonon and alloy disorder scattering are the dominant scattering processes) can be expressed as mere power-law expressions of the absolute energy. This allows one to define the temperature-dependent transport properties in terms of so-called Fermi integrals

$$F_j(\eta(T)) = \int_0^\infty \frac{\xi^j}{e^{\xi-\eta} + 1} d\xi. \quad (5)$$

Here, $\xi = E/(k_B T)$ and $\eta = \mu/(k_B T)$ represent the reduced energy and chemical potential, respectively. The temperature-dependent electrical conductivity, Seebeck coefficient and Hall coefficient, which can be simultaneously fitted in the *SeeBand* algorithm, can be most generally written for a single parabolic band as

$$S(T) = \frac{k_B}{e} \left[\eta - \frac{2F_1(\eta)}{F_0(\eta)} \right], \quad (6)$$

$$\rho(T) = \left[\frac{2\sqrt{2}e^2 k_B T}{\pi^2 \hbar^3} \left(\frac{\tilde{\tau}}{m} \right) T^\gamma F_0(\eta) \right]^{-1}, \quad (7)$$

$$R_H(T) = \frac{\pi^2 \hbar^3}{2e (2m k_B T)^{3/2}} \frac{F_{-1/2}(\eta)}{F_0^2(\eta)}. \quad (8)$$

Here, $\tilde{\tau}$ represents a reduced electron relaxation time, which depends for instance on the acoustic deformation or alloy disorder scattering potentials, m is the band effective mass and γ is a scattering-specific parameter which is -1 and 0 for acoustic phonon and alloy disorder scattering, respectively.

2.2. Multi-band and multi-carrier electronic transport

In the case that two or more parabolic bands end up contributing to the transport properties, the single-band contributions have to be weighted and summed up appropriately^{2,3} by the following relations

$$\sigma = \sum_i \sigma_i, \quad (9)$$

$$S = \frac{\sum_i S_i \sigma_i}{\sum_i \sigma_i}, \quad (10)$$

$$R_H = \frac{\sum_i R_{H,i} \sigma_i^2}{(\sum_i \sigma_i)^2}, \quad (11)$$

and

$$\kappa_e = T \sum_i L_i \sigma_i + T \left(\sum_i S_i^2 \sigma_i - \frac{(\sum_i S_i \sigma_i)^2}{\sum_i \sigma_i} \right). \quad (12)$$

In the above described theoretical framework, this leaves three independent fit parameters for the Seebeck coefficient in a two-band model, namely, the position of the Fermi energy with respect to the valence band edge E_F , the band gap or band overlap, i.e. the position of the conduction band bottom with respect to the valence band edge E_g as well as a conductivity weighting parameter $\epsilon_m = (m_1/m_2)^{-1}(\tau_1/\tau_2)(N_1/N_2)$, which includes the effective masses m_i , scattering times τ_i and degeneracies N_i of the two bands.

For the resistivity/conductivity, one additional fit parameter emerges, namely, the absolute scattering time of the valence band; the absolute scattering time of the conduction band can be calculated via the weighting parameter obtained during the Seebeck fit. Note that when two scattering processes, such as acoustic phonon and alloy disorder scattering are considered simultaneously, two additional fit parameters (the alloy disorder scattering potentials of the two respective bands) have to be introduced.

The Hall coefficient, allows for obtaining the absolute value of the effective masses in a final single-parameter fit. As described in Ref. ⁴, the *SeeBand* algorithm concurrently handles temperature-dependent data of the electrical resistivity, the Seebeck coefficient and the Hall coefficient for highly efficient and robust analyses of temperature-dependent transport and in order to deduce microscopic parameters regarding the electronic band structure and charge carrier scattering processes.

2.3. Modelling temperature-dependent transport in $\text{Fe}_2\text{V}_{0.95}\text{Ta}_{0.1}\text{Al}_{0.95}$

In Fig. S14, we show results of temperature-dependent analyses of all relevant transport properties for the Heusler material $\text{Fe}_2\text{V}_{0.95}\text{Ta}_{0.1}\text{Al}_{0.95}$, which has been used as a starting material for the high-performance composites. It can be seen that the Seebeck coefficient, the resistivity and the Hall coefficient can be simultaneously very well described using the very same band structure parameters, which hints at highly robust and reliable fitting results. These analyses reveal a narrow band gap of about 90 meV and rather heavy effective band masses for the conduction and valence band ($m_e = 8.5 m_0$ and $m_h = 9.7 m_0$). The latter most likely can be explained by the fact that the band structure of Fe_2VAl is highly complex when E_F is shifted from within the pseudogap – where mostly two bands (one at Γ and one at X) dominate the transport – into either the conduction or the valence band, where highly degenerate and non-parabolic bands are present. This is reflected also in a steep slope of the density of states at both the conduction and valence band side. Since the present sample is heavily doped ($n_H = 1.8 \times 10^{21} \text{ cm}^{-3}$) with E_F shifted deep into the conduction band states, we expect these non-parabolic bands to contribute to the transport as well.

Nonetheless, the fact that all transport properties can be simultaneously well described by this *effective* band structure model, allows us to visualize the individual contributions of the hole- and electron-like carriers to the total Seebeck coefficient (see Fig. S14d) and estimate the bipolar contribution to the electronic thermal conductivity (see Fig. S14e), the latter of which is crucial for determining the real value of the lattice thermal conductivity. Indeed, it can be seen in Fig. S14e, that the Wiedemann-Franz law insufficiently and inadequately captures the electronic contribution to the thermal conductivity at high temperatures. For instance, at $\approx 500 \text{ K}$, the bipolar term is already twice as large as compared to the Wiedemann-Franz term. However, Fig. S14f, where the theoretical upper limit of the dimensionless figure of merit for $\kappa_L \rightarrow 0$ is plotted and compared to experimental findings, clearly demonstrates that still lattice-dominated heat transport severely hampers the overall performance of these systems and there is significant room for improvement in terms of reducing κ_L , especially when a high weighted mobility can be retained.

3. Two-channel transport model for field-dependent Hall resistivity

In a two-channel transport model for two types of charge carriers with charge $q_{1,2}$, carrier density $n_{1,2}$ and carrier mobility $\mu_{1,2}$, the field-dependent longitudinal resistivity $\rho_{xx}(B)$ and Hall resistivity $\rho_{xy}(B)$ can be expressed as⁵

$$\rho_{xx}(B) = \frac{q_1 n_1 \mu_1 + q_2 n_2 \mu_2 + (q_1 n_1 \mu_2 + q_2 n_2 \mu_1) \mu_1 \mu_2 B^2}{(q_1 n_1 \mu_1 + q_2 n_2 \mu_2)^2 + (q_1 n_1 + q_2 n_2)^2 \mu_1^2 \mu_2^2 B^2} \quad (13)$$

and

$$\rho_{xy}(B) = \frac{q_1 n_1 \mu_1^2 + q_2 n_2 \mu_2^2 + (q_1 n_1 + q_2 n_2)^2 \mu_1^2 \mu_2^2 B^2}{(q_1 n_1 \mu_1 + q_2 n_2 \mu_2)^2 + (q_1 n_1 + q_2 n_2)^2 \mu_1^2 \mu_2^2 B^2} B. \quad (14)$$

From the above equations, it becomes obvious that non-linearities can occur in the field-dependent Hall resistivity. While previous models have employed four different fit parameters, i. e. the respective carrier densities and mobilities to model non-linear field dependencies, Eguchi and Paschen previously suggested a novel, more robust scheme for analyzing field-dependent magneto-transport properties⁶. This can be achieved by defining two new variables

$$N \equiv \frac{n_1 - n_2}{n_1 + n_2} \quad (15)$$

and

$$M \equiv \frac{\mu_1 - \mu_2}{\mu_1 + \mu_2}. \quad (16)$$

This allows rewriting Equation 13 and Equation 14 to the following new expressions, which depend on two, instead of four parameters

$$\begin{aligned} \rho_{xx}(B) &= \frac{2}{q_1 n_+ \mu_+} \\ &\times \frac{(1+N)(1+M) + \delta q(1-N)(1-M)}{[(1+N)(1+M) + \delta q(1-N)(1-M)]^2 + [(1+N) + \delta q(1-N)]^2 (1-M^2)^2 (\mu_+ B)^2} \\ &+ \frac{2}{q_1 n_+ \mu_+} \\ &\times \frac{[(1+N)(1-M) + \delta q(1-N)(1+M)](1-M)^2 (\mu_+ B)^2}{[(1+N)(1+M) + \delta q(1-N)(1-M)]^2 + [(1+N) + \delta q(1-N)]^2 (1-M^2)^2 (\mu_+ B)^2} \end{aligned} \quad (17)$$

and

$$\begin{aligned} \rho_{xy}(B) &= \frac{2}{q_1 n_+} \\ &\times \frac{(1+N)(1+M)^2 + \delta q(1-N)(1-M)^2 + [(1+N) + \delta q(1-N)](1-M)^2 (\mu_+ B)^2}{[(1+N)(1+M) + \delta q(1-N)(1-M)]^2 + [(1+N) + \delta q(1-N)]^2 (1-M^2)^2 (\mu_+ B)^2} B, \end{aligned} \quad (18)$$

with the auxiliary variables $\delta q \equiv q_2/q_1$ and n_+ and μ_+ defined as

$$n_+ \equiv \frac{2}{q_1 R_H} \left[\frac{(1+N)(1+M)^2 + \delta q(1-N)(1-M)^2}{[(1+N)(1+M) + \delta q(1-N)(1-M)]^2} \right] \quad (19)$$

and

$$\mu_+ \equiv \mu_H \frac{(1+N)(1+M) + \delta q(1-N)(1-M)}{(1+N)(1+M)^2 + \delta q(1-N)(1-M)^2}. \quad (20)$$

Here, R_H and μ_H are the Hall coefficient and Hall mobility in the linear response regime, i.e. $R_H = \lim_{B \rightarrow 0} \rho_{xy}/B$ and $\mu_H = \lim_{B \rightarrow 0} \rho_{xy}/(\rho_{xx} B)$, which can be obtained directly by performing a linear fit of the low-field experimental data.

Equation 18 was used to fit the experimental field-dependent ρ_{xy} data of the FVAB50 composite (Fig. 5b in the main manuscript) and to thereby extract the single-channel Hall mobilities $\mu_{1,2}$ and carrier concentrations $n_{1,2}$. As an additional consistency check and to confirm whether the fitted parameters are based on solid grounds, we compared the zero-field electrical resistivity $\rho_{xx}(T)$ obtained from temperature-dependent measurements with $\rho_{xx}(T)$ obtained when recalculating the resistivity from the obtained $\mu_{1,2}$ and $n_{1,2}$ fit parameters $\rho_{xx} = (e n_1 \mu_1 + e n_2 \mu_2)^{-1}$. Fig. S19 shows this "consistency check" and reveals that the recalculated zero-field resistivity is in very good agreement with the temperature-dependent measurements, which further strengthens the point that charge transport takes place via parallel conduction channels: (i) along the bulk $\text{Fe}_2\text{V}_{0.95}\text{Ta}_{0.1}\text{Al}_{0.95}$ matrix and (ii) along the $\text{Bi}_{1-x}\text{Sb}_x$ secondary phase at the grain boundaries.

4. Grain refinement and severe plastic deformation via high-pressure torsion

4.1. Attempts of reproducing high zT in $\text{Fe}_2\text{V}_{0.98}\text{Ta}_{0.1}\text{Al}_{0.92}$

In 2018, Masuda et al. reported on the effect of high-pressure torsion (HPT) on the microstructure and thermoelectric properties of Fe_2VAl -based full-Heusler compounds, achieving enhancements of the dimensionless figure of merit up to $zT = 0.3$ at around 500 K⁷. These enhancements were attributed to a reduction of the grain size during severe plastic deformation via HPT. Processing of thermoelectric materials via HPT has also been very effectively employed for skutterudites previously. For instance, Rogl et al. achieved an outstanding thermoelectric performance up to $zT > 2$ in multi-filled skutterudites^{8–10}. On the other hand, the authors found much less impressive enhancements of zT for half-Heusler compounds, when HPT has been employed to refine the grain size and introduce various defects such as dislocations^{11,12}. This can be ascribed to a strong tradeoff in carrier mobility and lattice thermal conductivity for the latter. In 2022, Fukuta and the same co-authors of Ref. 7, reported further enhancements of zT up to $zT = 0.37$ at around 400 K in $\text{Fe}_2\text{V}_{0.98}\text{Ta}_{0.1}\text{Al}_{0.92}$. These promising results, motivated us to (i) reproduce them and (ii) investigate other samples with different compositions to potentially realize even high thermoelectric performance. These experimental endeavours are summarized in this section.

Fig. S1 shows a comparison of experimental data by Fukuta et al. and data obtained in this work by following exactly the same synthesis and HPT processing conditions mentioned in Ref. ¹³. It can be seen that while the temperature-dependent Seebeck coefficient and thermal conductivity could be more or less well reproduced, the electrical resistivity found in the present study, is more than a factor of two larger than that reported in Ref. ¹³. Consequently, we were not able to realize an enhancement of zT in the present case. In fact, zT was even smaller than for the sample which was not subjected to HPT processing. This highlights, that exact setup-specific processing conditions during HPT are likely very important to realize the desired microstructure and properties.

4.2. Investigation of HPT processing of $\text{Fe}_2\text{V}_{0.95}\text{Ta}_{0.05}\text{Al}_{0.9}\text{Si}_{0.1}$ and other optimized full-Heusler systems

In order to determine whether enhancements of zT might be realizable for different Fe_2VAl -based Heusler compounds, we investigated a variety of samples with promising electronic properties (high power factor and weighted mobility) before and after HPT processing. Fig. S2 summarizes the evolution of the electronic transport properties ($S(T)$, $\rho(T)$ and $PF(T)$) of the recently discovered ultrahigh-PF compound $\text{Fe}_2\text{V}_{0.95}\text{Ta}_{0.05}\text{Al}_{0.9}\text{Si}_{0.1}$ ¹⁴. Again, similar to the afore-mentioned case of $\text{Fe}_2\text{V}_{0.98}\text{Ta}_{0.1}\text{Al}_{0.92}$, we observe a significant (factor 4) increase in the electrical resistivity, which persists even after several measurement-induced annealing cycles (see Fig. S2a). Simultaneously, the Seebeck coefficient decreases as a result of mechanically induced antisite disorder, which was confirmed by emergent magnetic behavior of the samples (not shown here). Fig. S2c and Fig. S2d show that the electrical resistivity progressively increases and the power factor progressively decreases as the number of revolutions during HPT increases. Thus, HPT turns out to be highly detrimental to the electronic transport properties, hindering improvements in the figure of merit. Virtually the same trend has been observed for all samples investigated and no enhancement of zT was realized even when the number of revolutions or the processing temperature during HPT were varied. Fig. S3 highlights that zT decreases after HPT as compared to the non-processed reference samples, pointing at a detrimental tradeoff between carrier weighted mobility (electronic scattering) and lattice thermal conductivity (phonon scattering). Going into the future, it will be essential to identify how to overcome this tradeoff and whether other groups are able to reproduce initial enhancements observed in Refs. ^{7,13}.

5. Additional micro- and nanostructure analyses of FVABX composites

5.1. TEM investigation near the Heusler–Bi–Sb grain boundary

Figure S6 illustrates TEM images acquired near the grain boundary (GB) of a FIB-fabricated sample. Panel (a) displays a bright-field image where the Fe_2VAl grain and the Bi–Sb grain are separated by the GB. Panel (b) shows a lattice image near the GB, while panel (c) presents the FFT of the area limited by the yellow square. Panel (d) depicts a simulation of Selected Area Diffraction (SAD) result adopting the ReciPro software. Panels (e) and (f) demonstrate an inverse FFT of panel (c), choosing spots 022 and $\overline{0}2\overline{2}$ for panel (e) and spots $\overline{1}1\overline{1}$ and $1\overline{1}1$ for panel (f), respectively. Interplanar distances are identified

by measuring distances between successive fringes; distances between 10 successive fringes are measured and displayed in panels (e) and (f). Panel (g) provides a low-magnification TEM image of an area including Fe_2VAl and Bi-Sb grains, along with a Ta-rich precipitate. Panel (h) shows a lattice image of the Ta-rich precipitate acquired in the area marked by the yellow square in panel (g), showing an interplanar distance of approximately 6.4 \AA , which is a twofold difference compared to that of the Fe_2VAl phase. Panels (i) and (k) are SAD patterns acquired at the Ta-rich precipitate and Fe_2VAl grain, respectively, along the $[211]$ zone-axis. These figures indicate that the Ta-rich precipitate has a superstructure of the Heusler phase with a nearly similar crystal orientation, suggesting a relationship in the formation of the Fe_2VAl phase and the Ta-rich precipitate. A light ring, indicated by a yellow arrow in panel (i), is attributed to an amorphous phase, likely covering the Ta-rich precipitate. Panel (l) shows a lattice image of one of the nanograins, whose phases are unidentified, observed inside the $\text{Bi}_{1-x}\text{Sb}_x$ grain and near the Ta-rich precipitate, marked by the blue dashed ellipse in panel (h).

5.2. TEM investigation of a Heusler grain

Figure S7 presents Transmission Electron Microscopy (TEM) images of a powder sample, which was obtained by crushing a sintered sample. Panel (a) shows a lattice image of one of the grains, highlighting its atomic arrangement. A more detailed view is provided in panel (b), which displays a high-magnification image of the region outlined by the yellow square in panel (a). Here, interplanar distances of approximately 2.0 \AA , characteristic of the Fe_2VAl phase, are observed. The corresponding fast Fourier transform (FFT) of this region is shown in panel (c), providing insight into the crystallographic order of the grain. Panel (d) presents a simulation of the selected area diffraction (SAD) pattern along the $[100]$ zone-axis, offering further confirmation of the crystal structure. In panel (e), another grain is displayed with its atomic lattice clearly visible. A high-magnification image of the yellow-square region from panel (e) is depicted in panel (f), showing interplanar distances of approximately 3.3 \AA for the Fe_2VAl phase. The FFT of this region is provided in panel (g), while panel (h) reveals an inverse FFT of panel (g). The green circles in panel (g) mark specific spots in the FFT, indicating several dislocation defects, which are made more evident in the inverse FFT image in panel (h). These defects are of particular interest for understanding the local structural characteristics of the Fe_2VAl phase.

6. Acoustic mismatch in the phonon band structures and densities of states of elemental Bi and Heusler-type Fe_2VAl

Fig. S20 compares phonon band structures and densities of states of Heusler-type Fe_2VAl and elemental Bi. The strong mismatch in the acoustic properties is reflected in a significantly flattened phonon dispersion for Bi when compared to Fe_2VAl . This can be mainly attributed to the much higher atomic mass of Bi compared to Fe, V and Al. Indeed, as follows already in a simple model for a one-dimensional monoatomic chain, the dispersion relation $\omega(k)$ can be expressed as

$$\omega(k) = 2\sqrt{\frac{K}{m}} \sin\left(\frac{1}{2}ka\right). \quad (21)$$

Here, K represents a spring force constant acting on the atoms, m the atomic mass and a the interatomic spacing. While the acoustic branches of Fe_2VAl reach up to about 9 THz and the highest lying optical branches reach a bit more than 12 THz, the phonon spectrum of elemental Bi is capped at frequencies less than 4 THz. This leads to an ≈ 9 THz mismatch in the phonon densities of states of the two respective materials. Although substitution with Ta in $\text{Fe}_2\text{V}_{1-x}\text{Ta}_x\text{Al}$ or Sb in $\text{Bi}_{1-x}\text{Sb}_x$ could slightly change the phonon spectra (W substitution in $\text{Fe}_2\text{V}_{1-x}\text{W}_x\text{Al}$ has been reported to lead to a 6 and 10 % reduction of the sound velocities for $x = 0.125$ and $x = 0.25$, respectively¹⁵), the qualitatively large difference between the two chemically distinct materials is expected to be the same. This phonon mismatch is also reflected in substantially different Debye temperatures and sound velocities (see also Fig. S20c): $\Theta_D \approx 120 \text{ K} / v_l \approx 2240 \text{ m s}^{-1}$ for elemental Bi and even lower $\Theta_D \approx 90 \text{ K} / v_l \approx 1990 \text{ m s}^{-1}$ for $\text{Bi}_{0.9}\text{Sb}_{0.1}$ ¹⁶ but much higher $\Theta_D \approx 540 \text{ K} / v_l \approx 6380 \text{ m s}^{-1}$ for Fe_2VAl ¹⁷. Such large mismatching phonon dispersions can be very effective in reducing lattice thermal conductivity in composite materials. The idea is that when a phonon crosses the heterogeneous interface between the two distinct materials, only phonons with matching densities of states are allowed to pass through, effectively filtering phonons in the mismatching energy spectrum. This leads to an extremely large thermal grain boundary resistance. The prospect of engineering such mismatching phonon modes in composite materials has been reported previously, e.g., in Cu_2Se –graphene¹⁸, Bi_2Te_3 –PEDOT:PSS¹⁹ and other composite systems^{20–22}.

7. Isotropy of thermal transport confirmed by measurements in different directions of the sample

Commonly, in thermoelectric materials prepared via sintering, the thermal conductivity is measured parallel to the compaction direction, whereas the electronic transport properties (resistivity and Seebeck coefficient) are usually measured only perpendicular to the direction of compaction. This can lead to erroneous estimates of the dimensionless figure of merit when the material displays anisotropy in its microstructure or crystal structure, and thus, in its transport properties. For instance, Kim et al. reported in 2015 extraordinarily high values of the dimensionless figure of merit up to $zT = 1.86$ at 320 K in $(\text{Bi}, \text{Sb})_2\text{Te}_3$ alloys prepared via liquid-phase sintering²³. However, it was shown a couple of years later by Rigui et al. that these high zT values probably result erroneously from a favorable but incorrect combination of thermal conductivity measured along the compaction direction of a sintered sample with an anisotropic microstructure, while charge transport is measured in the direction perpendicular to the compaction direction²⁴.

To rule out any anisotropy of thermoelectric transport in our composite samples, we measured the thermal conductivity in different directions of the sample using different techniques (see Fig. S21). Excellent agreement between low-temperature measurements performed perpendicular to the pressing direction, using a steady-state method, and high-temperature measurements performed parallel to the pressing direction, using a laser flash

diffusivity method, confirm that the microstructure of our samples does not display any 382
sizeable anisotropy which might affect the thermal conductivity in a similar manner to that 383
reported in Ref. ²³. 384

8. Supplementary Figures

8.1. HPT-deformed $\text{Fe}_2\text{V}_{0.98}\text{Ta}_{0.1}\text{Al}_{0.92}$: a comparison to literature

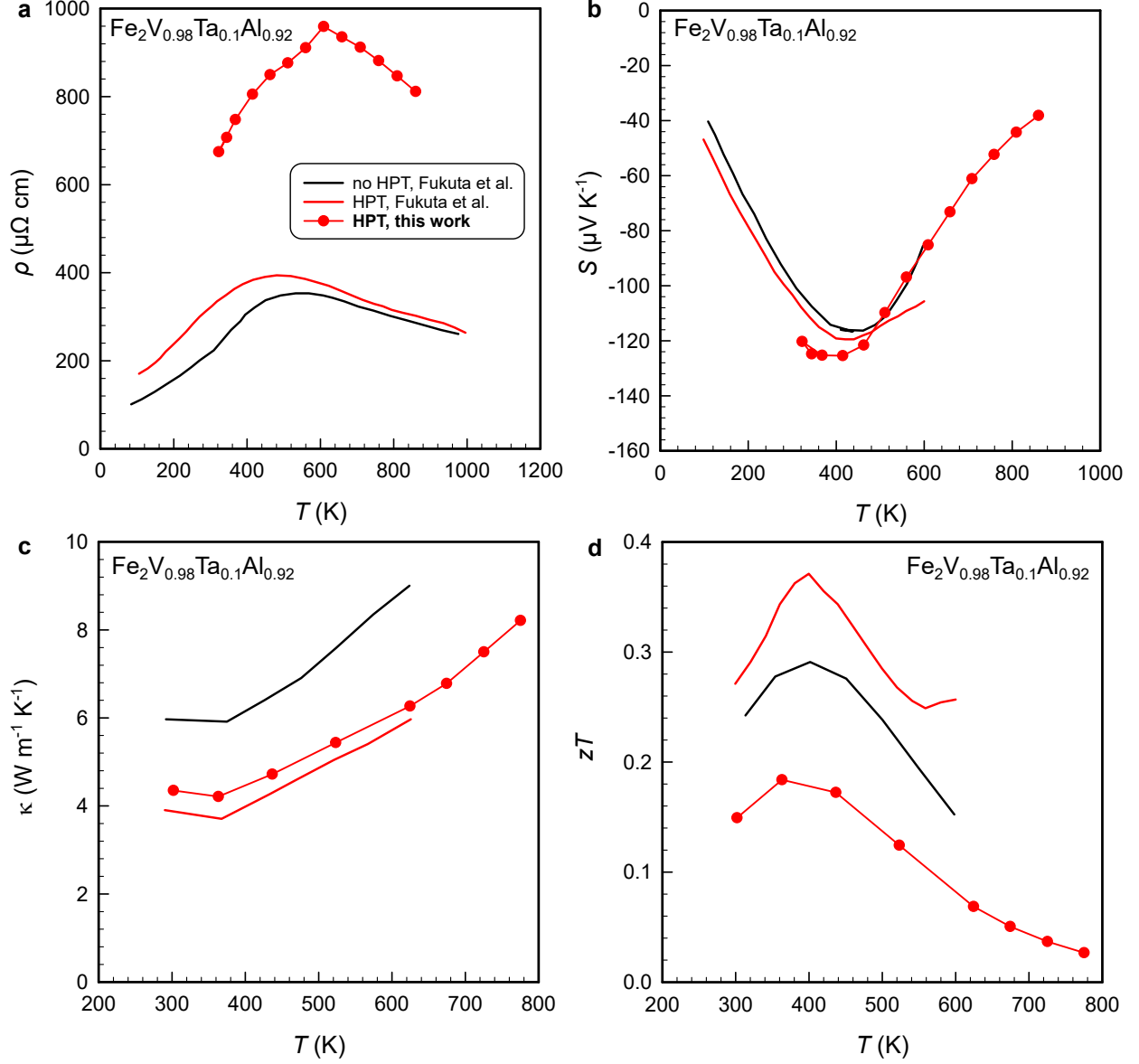


Fig. S1 | Thermoelectric properties of $\text{Fe}_2\text{V}_{0.98}\text{Ta}_{0.1}\text{Al}_{0.92}$ plastically deformed via high pressure torsion (HPT). a, Electrical resistivity, b, Seebeck coefficient, c, thermal conductivity and d, dimensionless figure of merit. Experimental data obtained within this study are compared to those by a recent study by Fukuta et al.¹³. While the Seebeck coefficient and thermal conductivity can be well reproduced, the electrical resistivity is significantly higher in this work, leading to an almost two times smaller zT .

8.2. Effect of HPT on electronic transport in $\text{Fe}_2\text{V}_{0.95}\text{Ta}_{0.05}\text{Al}_{0.9}\text{Si}_{0.1}$

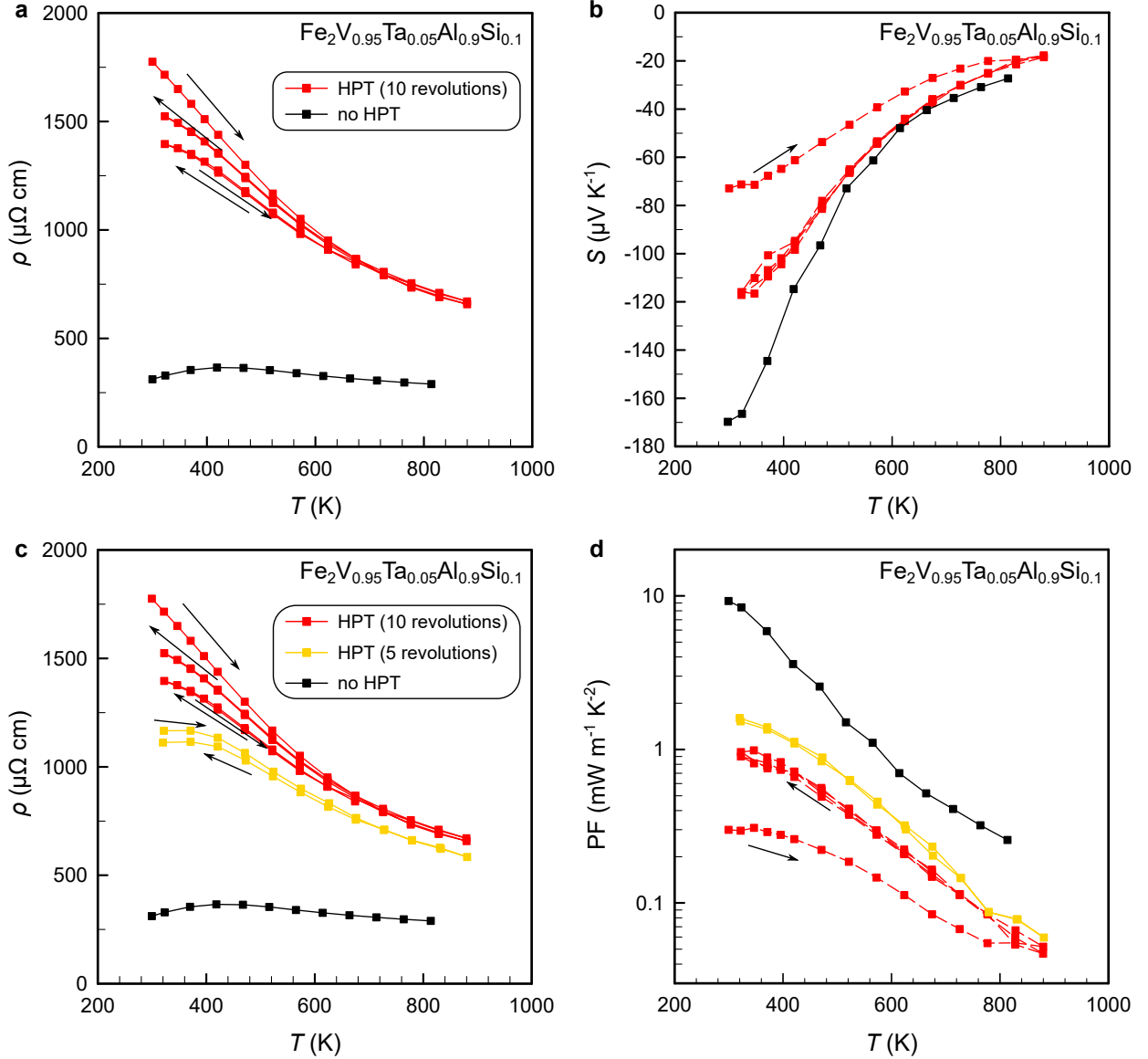


Fig. S2 | Effect of high-pressure torsion (HPT) on the thermoelectric properties of $\text{Fe}_2\text{V}_{0.95}\text{Ta}_{0.05}\text{Al}_{0.9}\text{Si}_{0.1}$. a, Temperature-dependent electrical resistivity and b, Seebeck coefficient of $\text{Fe}_2\text{V}_{0.95}\text{Ta}_{0.05}\text{Al}_{0.9}\text{Si}_{0.1}$ before and after HPT treatment with 10 revolutions. Several heating and cooling cycles are shown until the properties reach an equilibrium. c, Temperature-dependent electrical resistivity and d, power factor ($\text{PF} = S^2/\rho$) before and after HPT. The electrical resistivity increases substantially and PF decreases with the number of revolutions during HPT due to an increase in the defect density comprising atomic-scale antisite disorder, nano-scale dislocations and grain size reduction.

8.3. Effect of HPT processing for different Heusler samples

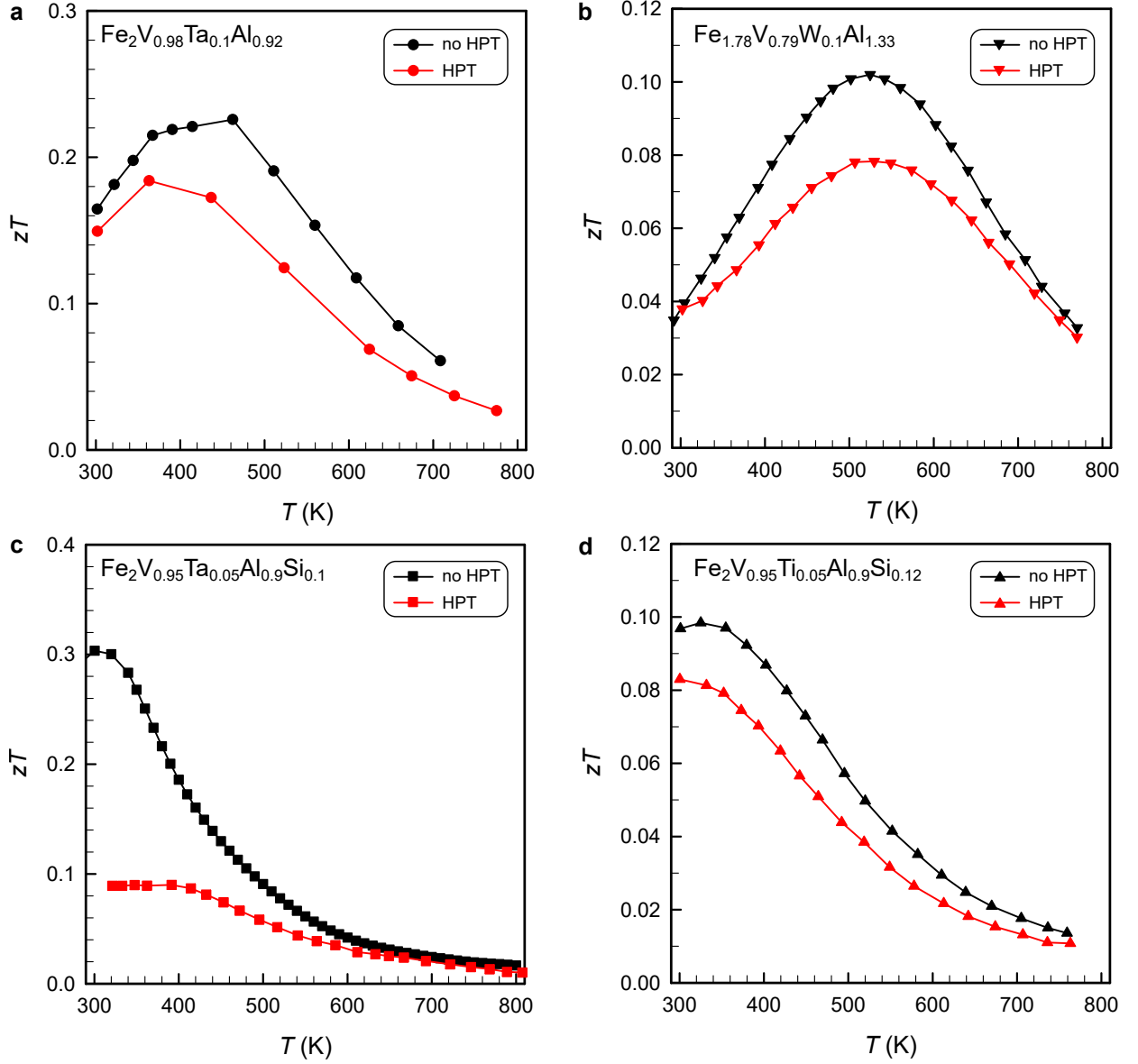


Fig. S3 | Comparison of dimensionless figure of merit of different Fe_2VAl -based full-Heusler compounds with optimized composition before and after HPT. Temperature-dependent figure of merit before and after HPT (10 revolutions) for **a**, off-stoichiometric and Ta-substituted $\text{Fe}_2\text{V}_{0.98}\text{Ta}_{0.1}\text{Al}_{0.92}$, **b**, off-stoichiometric and W-substituted $\text{Fe}_{1.78}\text{V}_{0.79}\text{W}_{0.1}\text{Al}_{1.33}$, **c**, Ta- and Si-co-substituted $\text{Fe}_2\text{V}_{0.95}\text{Ta}_{0.05}\text{Al}_{0.9}\text{Si}_{0.1}$ and **d**, Ti- and Si-co-substituted $\text{Fe}_2\text{V}_{0.95}\text{Ti}_{0.05}\text{Al}_{0.9}\text{Si}_{0.12}$.

8.4. Additional microstructure investigation of $\text{Fe}_2\text{V}_{0.95}\text{Ta}_{0.1}\text{Al}_{0.95}$

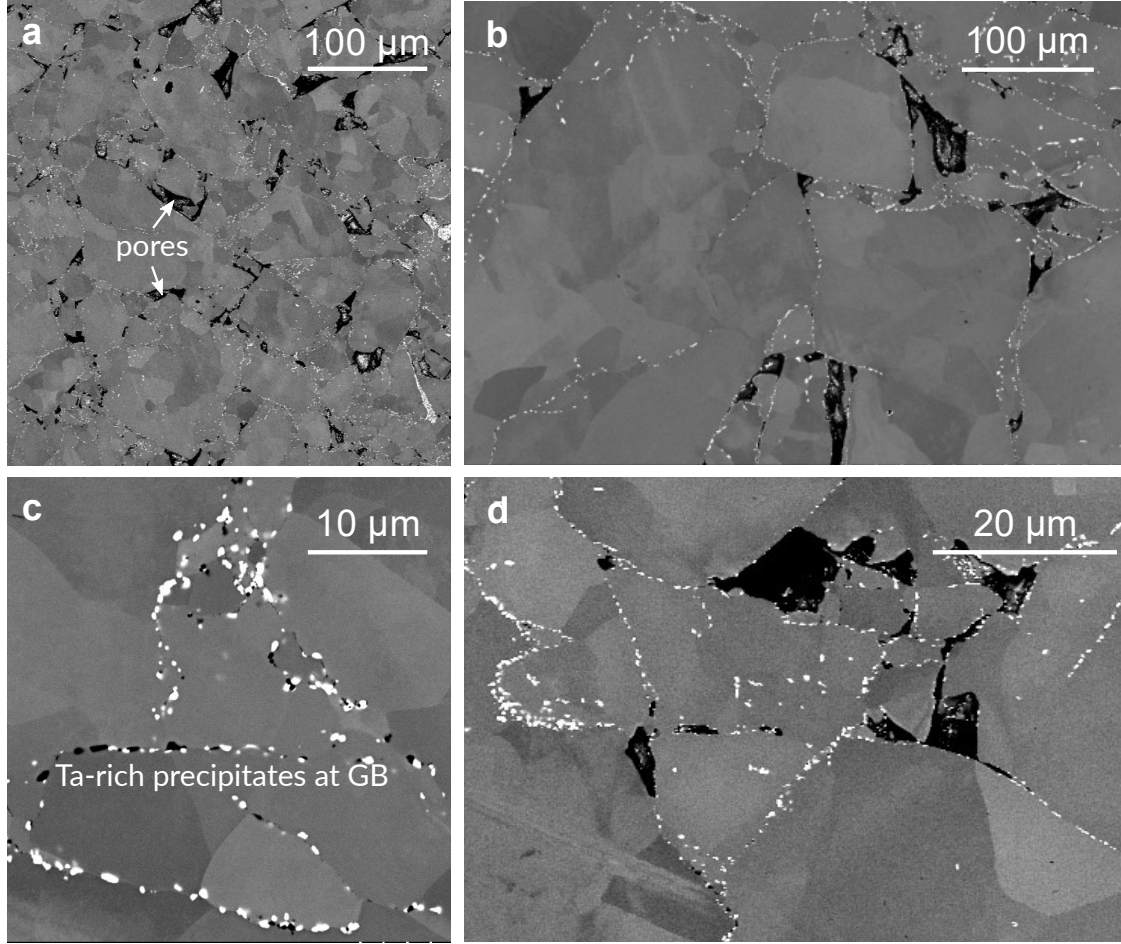


Fig. S4 | Microstructures of pristine $\text{Fe}_2\text{V}_{0.95}\text{Ta}_{0.1}\text{Al}_{0.95}$ (FVAB0) probed by backscattered scanning electron microscopy. **a,b**, BS-SEM images at low magnification at different areas of the same sample reveal pores evenly distributed throughout the whole sample. **c,d**, High-magnification BS-SEM images at different areas of the same sample reveal small, Ta-rich precipitates which segregate at the grain boundaries, likely already during the melt-synthesis in the induction furnace and further upon annealing during the high-temperature sintering process.

8.5. Focused ion beam preparation of FVAB50 composite near a Heusler- $\text{Bi}_{1-x}\text{Sb}_x$ grain boundary

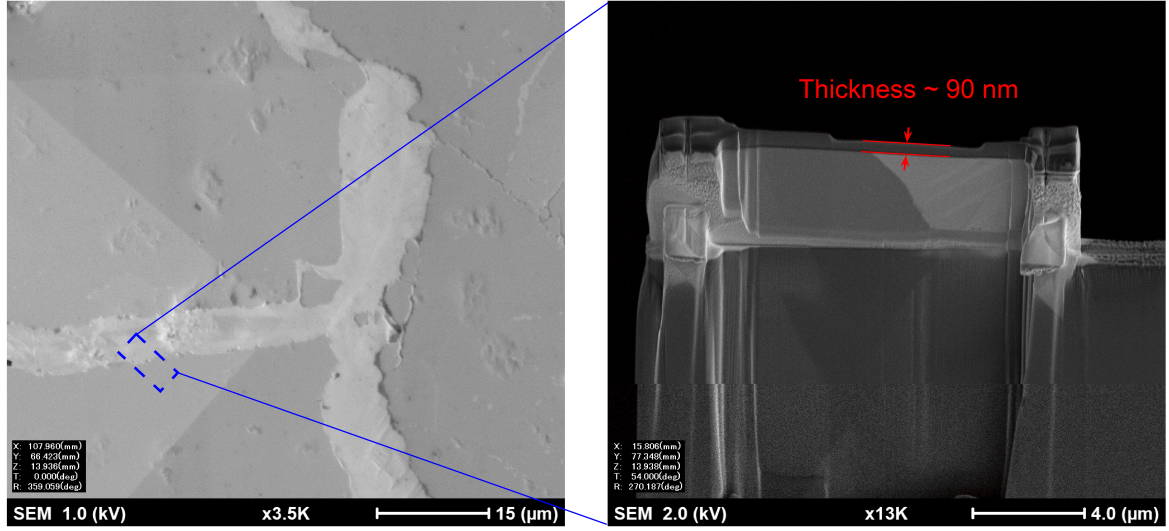


Fig. S5 | Focused ion beam preparation of a FVAB50 composite sample near the grain boundary of the Heusler phase and $\text{Bi}_{1-x}\text{Sb}_x$.

8.6. Additional TEM investigation of a FIB-fabricated sample near the Heusler- $\text{Bi}_{1-x}\text{Sb}_x$ grain boundary

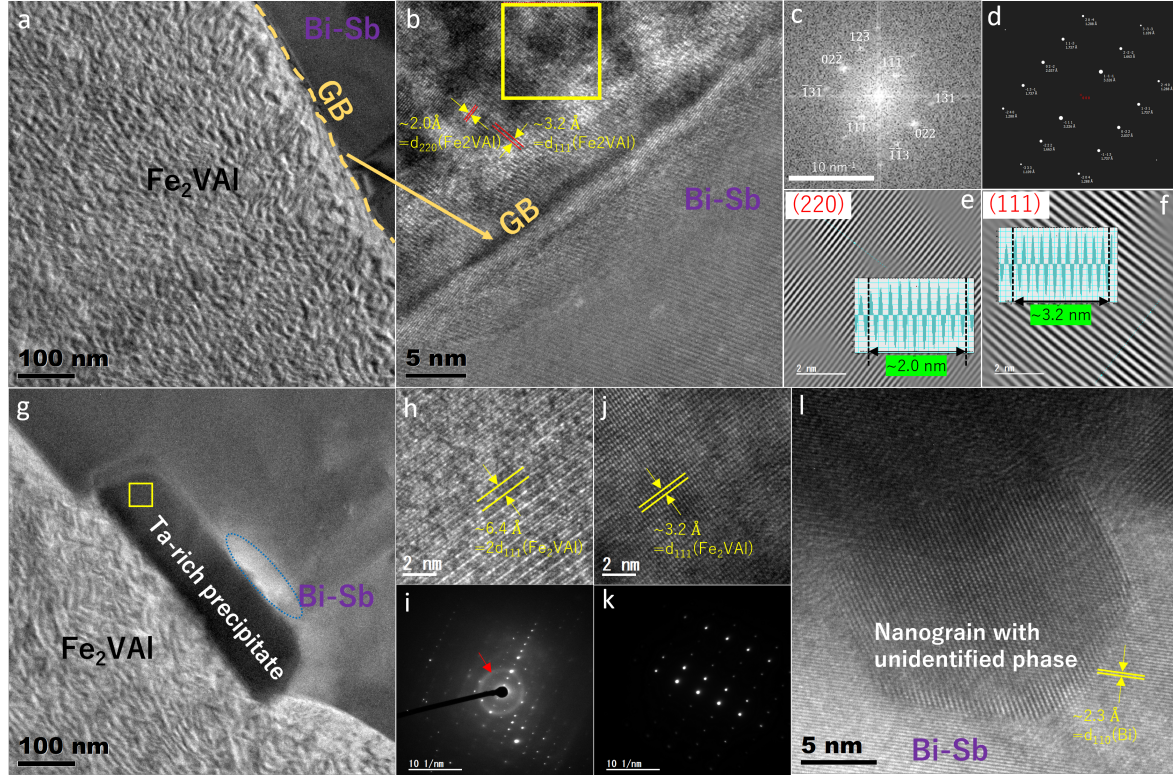


Fig. S6 | Transmission electron microscopy of an FIB-fabricated specimen near the grain boundary of the Heusler phase and $\text{Bi}_{1-x}\text{Sb}_x$. **a**, Bright-field image showing the Fe_2VAI grain and the Bi-Sb grain, separated by a grain boundary (GB). **b**, Lattice image taken near the GB. **c**, FFT of the region highlighted by the yellow square. **d**, Simulated Selected Area Diffraction (SAD) pattern using Recipro. **e** and **f**, Inverse FFT images derived from panel **c**, where panel **e** corresponds to the selection of spots 0-22 and 02-2, and panel **f** corresponds to spots -111 and 1-1-1. Interplanar distances are determined by measuring the spacing between successive fringes, with distances between 10 fringes shown in panels **e** and **f**. **g**, Low-magnification TEM image capturing Fe_2VAI and Bi-Sb grains, alongside a Ta-rich precipitate. **h**, Lattice image of the Ta-rich precipitate taken from the area marked by the yellow square in panel **g**, revealing an interplanar distance of approximately 6.4 Å, double that of the Fe_2VAI phase. **i** and **k**, SAD patterns obtained from the Ta-rich precipitate and Fe_2VAI grain, respectively, along the [211] zone-axis. These results indicate that the Ta-rich precipitate has a Heusler superstructure with nearly the same crystal orientation as the Fe_2VAI grain, suggesting a relationship in their formation. The light ring in panel **i**, marked by a red arrow, likely corresponds to an amorphous phase covering the Ta-rich precipitate. **l**, Lattice image of a nanograin (phase unidentified) within the Bi-Sb grain and near the Ta-rich precipitate, as indicated by the blue dashed ellipse in panel **g**.

8.7. Additional high-resolution TEM of Heusler grains in FVAB50

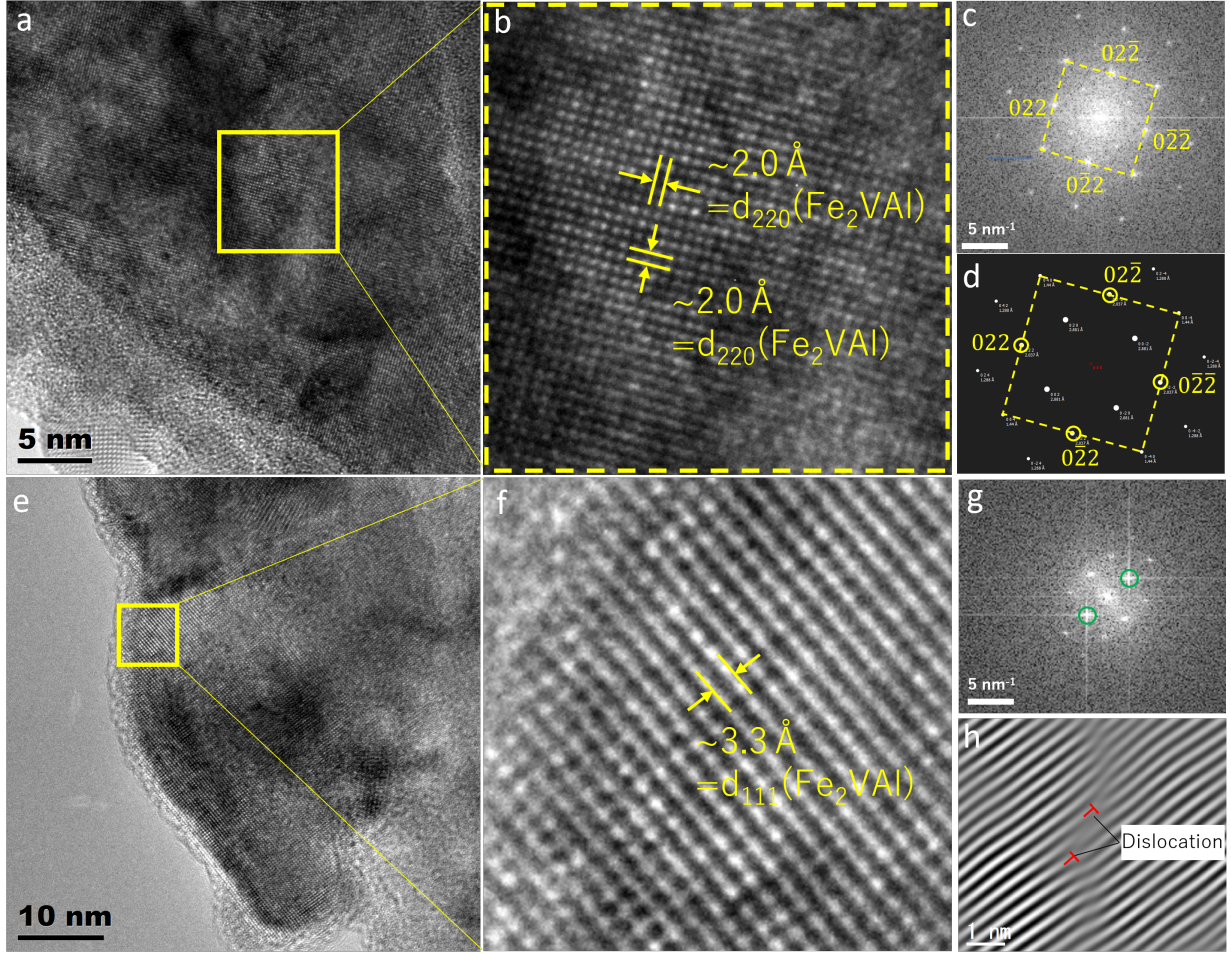


Fig. S7 | Transmission electron microscopy (TEM) of a grain of the FVAB50 composite conducted on powder of a crushed sintered sample. **a**, Lattice image of a grain of the Heusler phase. **b**, High-magnification image of the area delimited by a yellow square in **a**, revealing interplanar distances of approximately 2.0 Å of the Fe_2VAI phase. Panel **c** depicts the FFT of **b**. **d**, Simulation of the SAD pattern along the [100] zone-axis. **e**, Lattice image of another grain. **f**, High-magnification image of the area delimited by a yellow square in **e**, showing an interplanar distance of approximately 3.3 Å of the Fe_2VAI phase. Panel **g** shows the FFT of **f**. **h**, Inverse FFT of **g**, where spots marked by green circles in **g** indicate several dislocation defects.

8.8. EDX spectroscopy of nanoscale precipitates

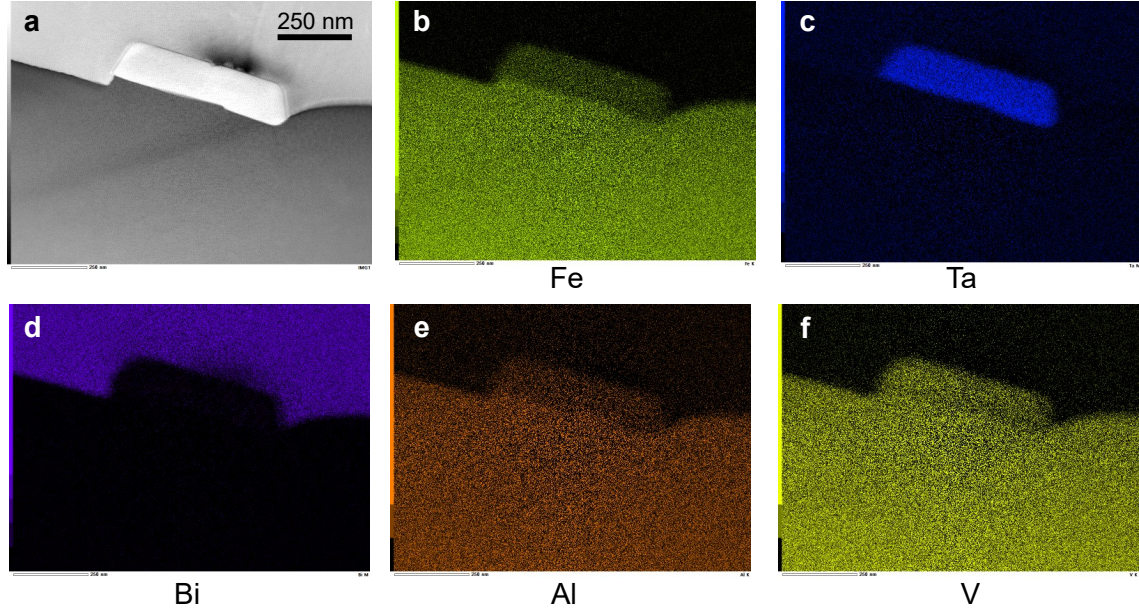


Fig. S8 | Energy-dispersive X-ray spectroscopy of a Ta-rich precipitate at the Heusler-Bi_{1-x}Sb_x interface. **a**, STEM image **b-f**, EDX mapping of Fe, Ta, Bi, Al and V, respectively, reveals a precipitate which is rich in Ta but contains also all other elements of the Heusler phase, namely Fe, V and Al. The composition of the precipitate is obtained as 39.8 at.% Ta, 28.2 at.% Fe, 19.3 at.% V, 12.7 at.% Al.

8.9. Additional EDX analysis of two-phase microstructures

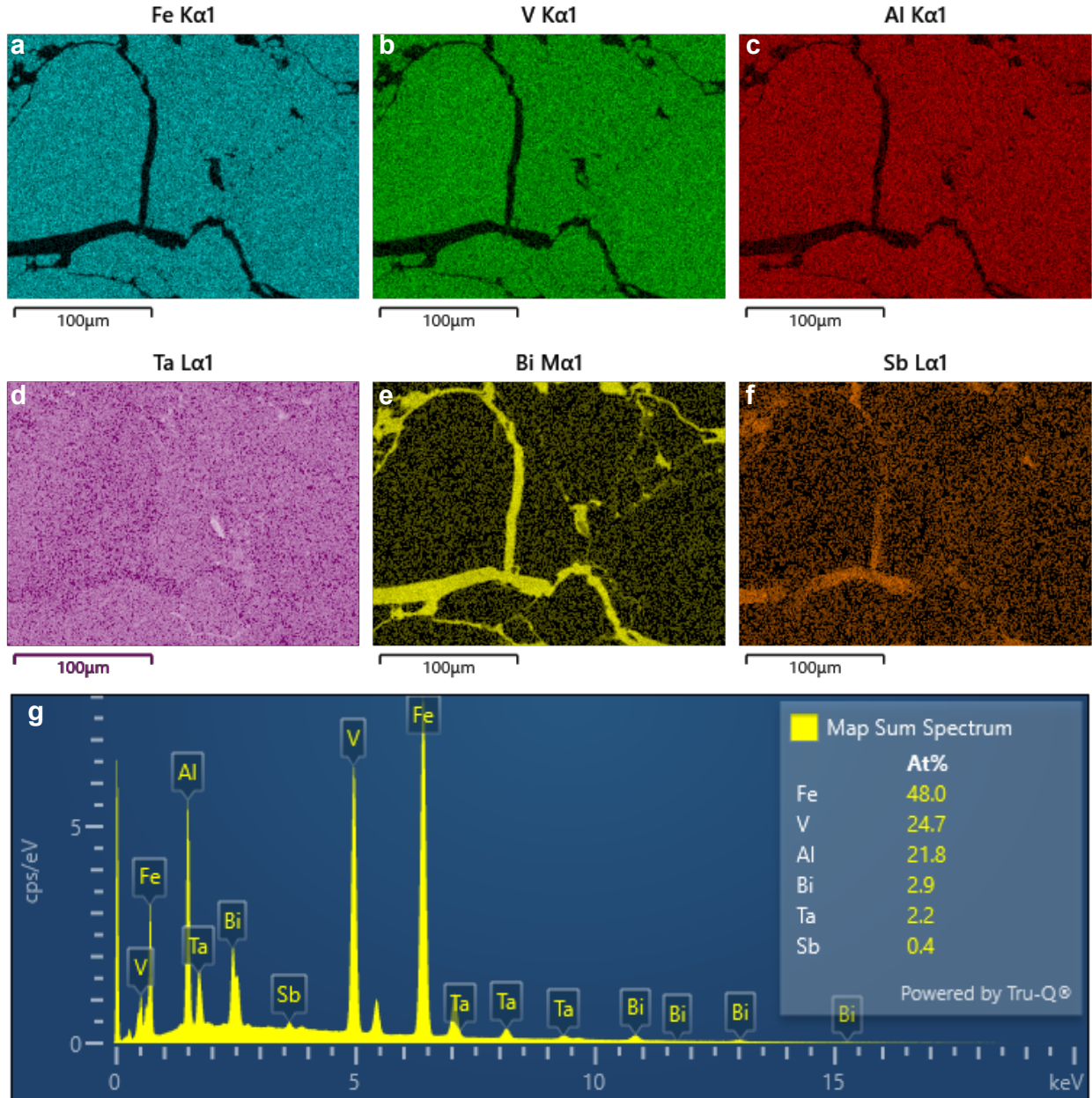


Fig. S9 | Additional energy-dispersive X-ray spectroscopy of FVABX composites. a-f Elemental mappings of Fe, V, Al, Ta, Bi and Sb, respectively. Variations in the Sb concentration within the $\text{Bi}_{1-x}\text{Sb}_x$ secondary phase are apparent and indicate that the composition of $\text{Bi}_{0.9}\text{Sb}_{0.1}$ changes during liquid-phase sintering and depends on the local surrounding in the sample. g, EDX spectrum with contributions of the different elements in atomic percent.

8.10. Additional SEM analysis of FVABX composites

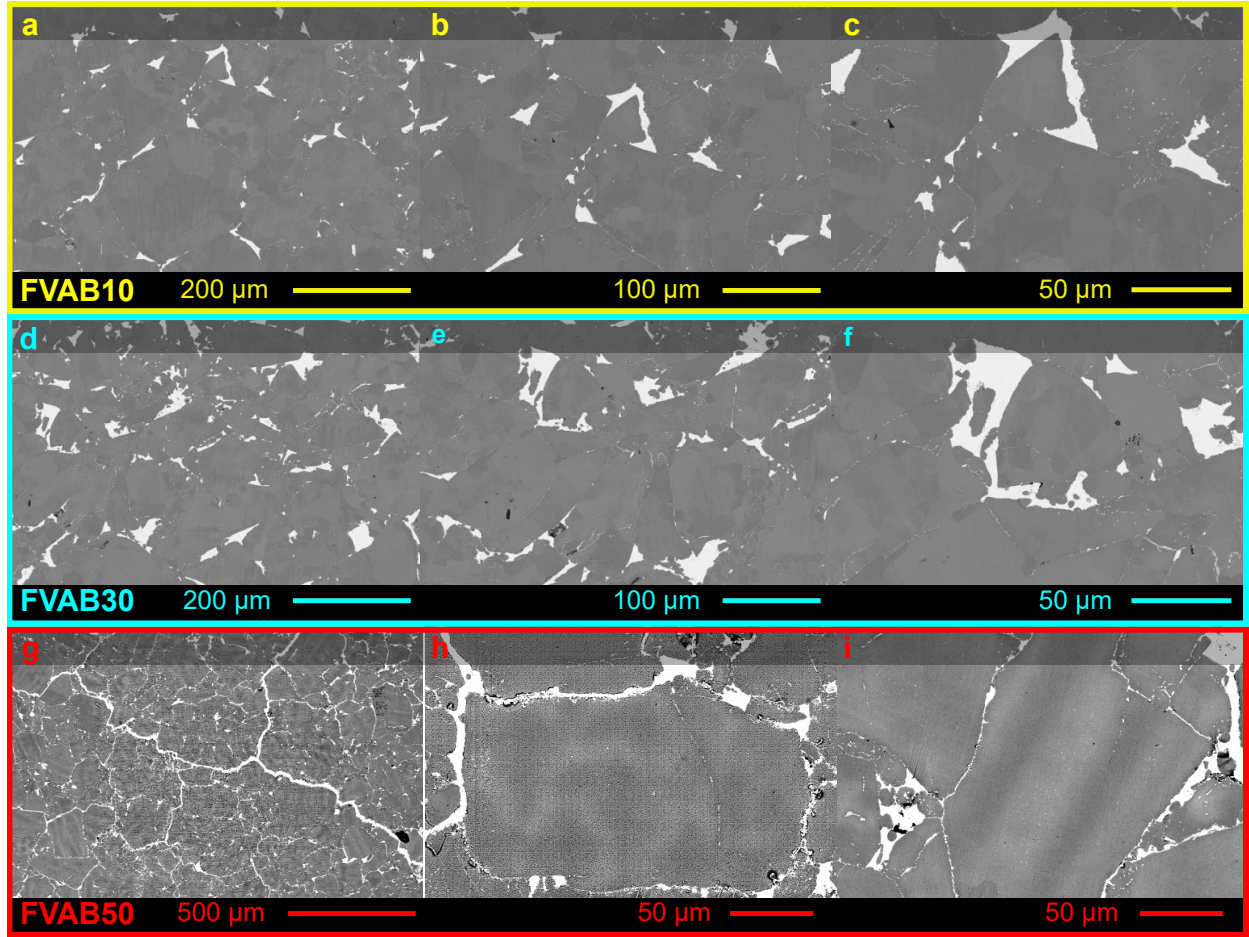


Fig. S10 | Additional backscattered electron micrographs of FVABX composites. **a-c**, BSE-SEM images of FVAB10 (10 vol.% $\text{Bi}_{0.9}\text{Sb}_{0.1}$ added before sintering), **d-f**, FVAB30 (30 vol.% $\text{Bi}_{0.9}\text{Sb}_{0.1}$ added before sintering) and **g-i**, FVAB50 (50 vol.% $\text{Bi}_{0.9}\text{Sb}_{0.1}$ added before sintering), at different magnifications. It can be seen that, initially, only the triple junctions between the Heusler grains are filled with the secondary phase, whereas a coherent and connected network of $\text{Bi}_{1-x}\text{Sb}_x$ develops for the latter. Simultaneously, a patterned microstructure, with brightness variations inside the Heusler grains corresponding to Ta-supersaturated regions, emerges.

8.11. Quantitative analysis of Bi/Sb concentrations in FVABX composites

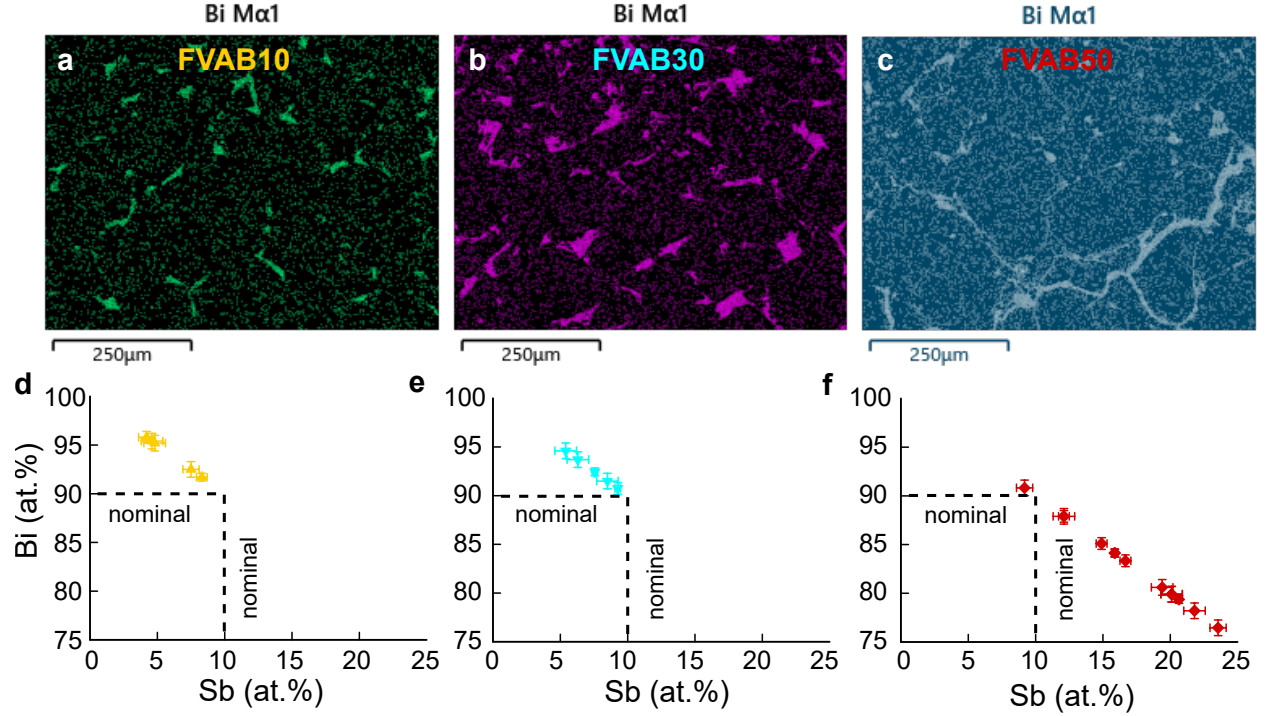


Fig. S11 | EDX mapping and composition analysis of the secondary phase. a-c, EDX mapping of Bi in FVAB10, FVAB30 and FVAB50 composites, respectively. d-f shows Bi and Sb concentrations obtained from EDX mapping and point analyses at various different spots in the sample. Interestingly, these results suggest that the Sb concentration increases when the amount of $\text{Bi}_{0.9}\text{Sb}_{0.1}$ powder added before sintering is increased. Moreover, the composition of the secondary phase fluctuates at the microscale throughout the sample (cf. also Fig. S9f).

8.12. X-ray powder diffraction patterns

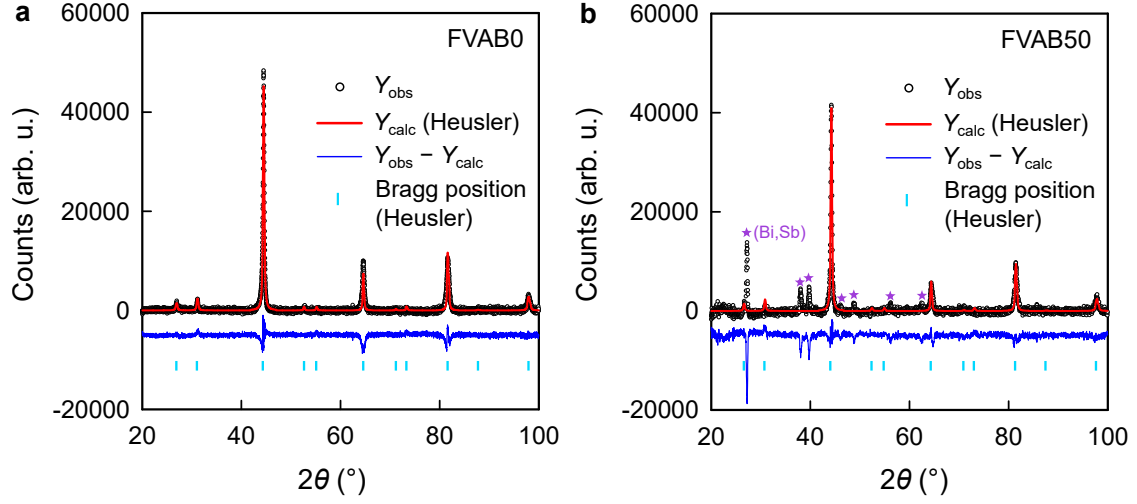


Fig. S12 | X-ray powder diffraction patterns of FVAB0 and FVAB50. **a**, XRD pattern of the pure Heusler sample with the nominal composition $\text{Fe}_2\text{V}_{0.95}\text{Ta}_{0.1}\text{Al}_{0.95}$. Red solid line shows a Rietveld refinement, from which the lattice parameter was derived as $a = 0.578(4)$ nm. **b**, XRD pattern for the high-performance FVAB50 composite sample, which was prepared via liquid phase sintering by adding 50 vol.% $\text{Bi}_{0.9}\text{Sb}_{0.1}$ powder before the compaction process. The Rietveld refinement on the main matrix is shown as a red solid line and reveals a clearly increased lattice parameter of $a = 0.579(3)$ nm, which is associated with an enhanced solubility limit of Ta in the Heusler structure.

8.13. Comparison of the temperature-dependent Seebeck coefficient of polycrystalline $\text{Bi}_{0.9}\text{Sb}_{0.1}$ with literature

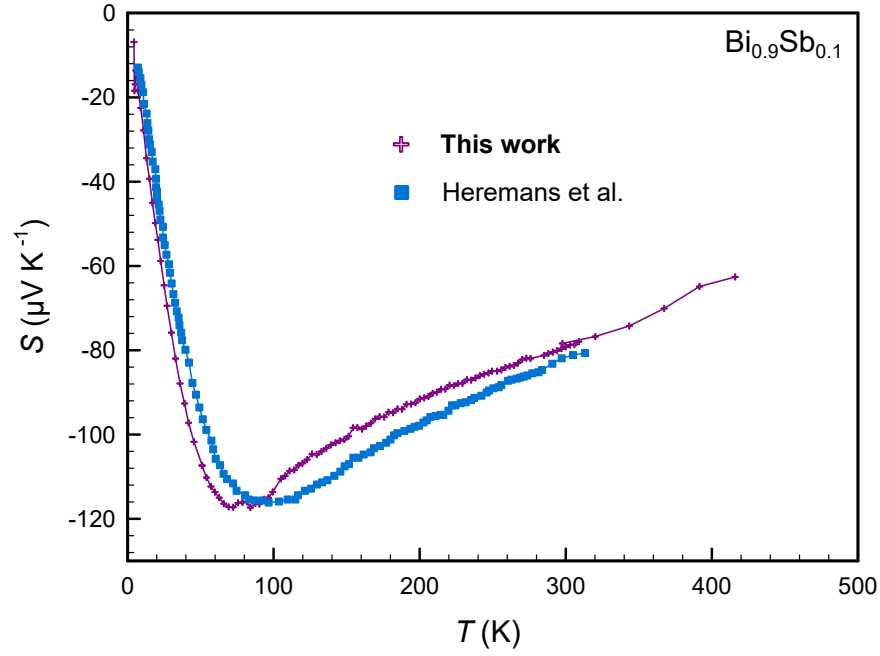


Fig. S13 | Consistency check with previous work. Comparison of the temperature-dependent Seebeck coefficient of polycrystalline $\text{Bi}_{0.9}\text{Sb}_{0.1}$ from this study and data obtained previously by Heremans et al.²⁵.

8.14. Constructing an effective band structure model for $\text{Fe}_2\text{V}_{0.95}\text{Ta}_{0.1}\text{Al}_{0.95}$

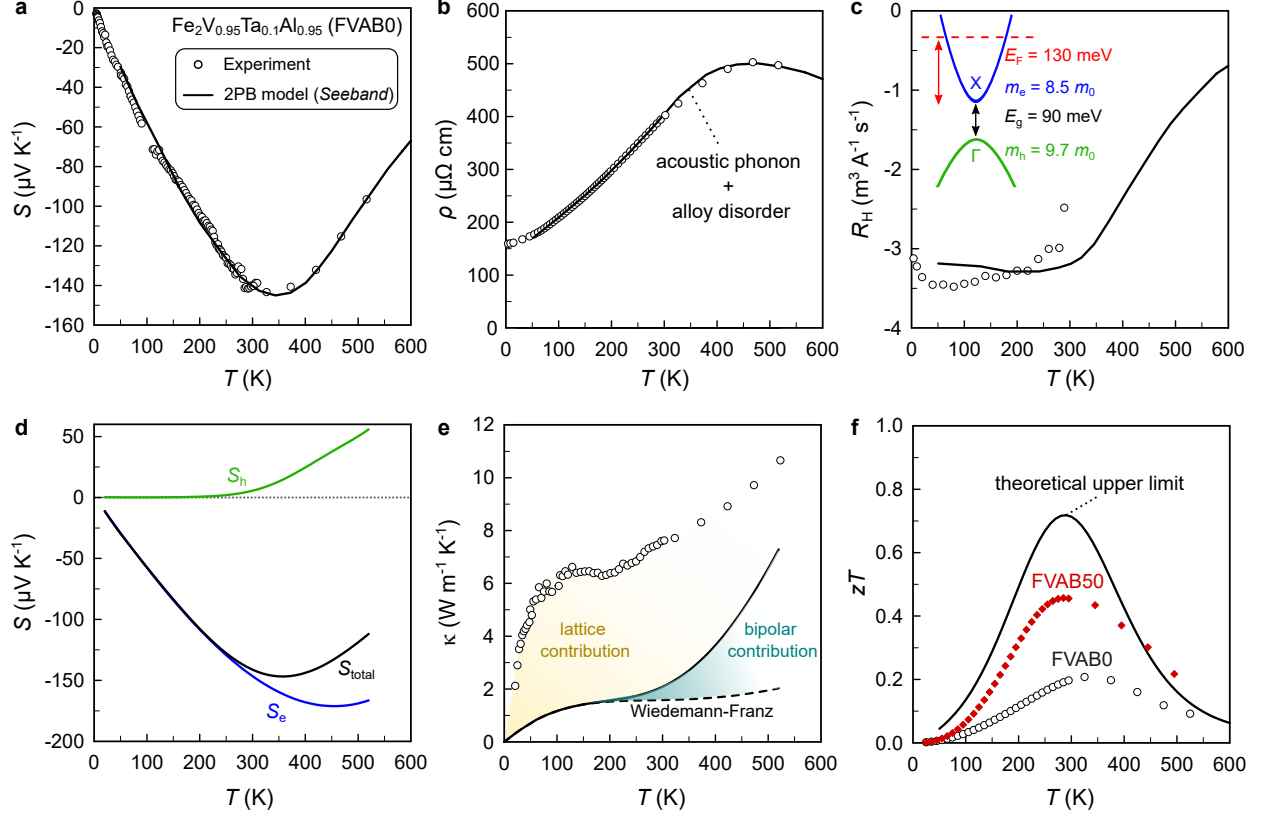


Fig. S14 | Modelling temperature-dependent electronic transport in Heusler-type $\text{Fe}_2\text{V}_{0.95}\text{Ta}_{0.1}\text{Al}_{0.95}$. **a**, Temperature-dependent Seebeck coefficient **b**, electrical resistivity and **c**, Hall coefficient. Solid lines are least-squares fits employing a two-parabolic band model, as implemented in the *SeeBand* fitting algorithm⁴. Two different scattering mechanisms have been considered: (i) Charge carrier scattering off acoustic phonons and (ii) alloy disorder scattering arising from Ta substitution and off-stoichiometry. The inset in **c** shows a sketch of the band structure. **d**, Total and individual band contributions to the temperature-dependent Seebeck coefficient. **e**, Temperature-dependent thermal conductivity. Solid line represents the total electronic part including the bipolar contribution, which can be calculated when $S(T)$, $\rho(T)$ and $R_H(T)$ are appropriately described within the electronic band structure model. Dashed line depicts the Wiedemann-Franz term of the electronic part, which significantly deviates from the total electronic contribution at high temperatures. **e**, Temperature-dependent zT from experiments and theoretical curve predicted by the two-band model in the limit that $\kappa_L \rightarrow 0$ (solid line). Experimental data of FVAB50 composite are also added for comparison.

8.15. Temperature-dependent Seebeck modelling of $\text{Bi}_{0.9}\text{Sb}_{0.1}$ and $\text{Fe}_2\text{V}_{0.95}\text{Ta}_{0.1}\text{Al}_{0.95}$ starting materials

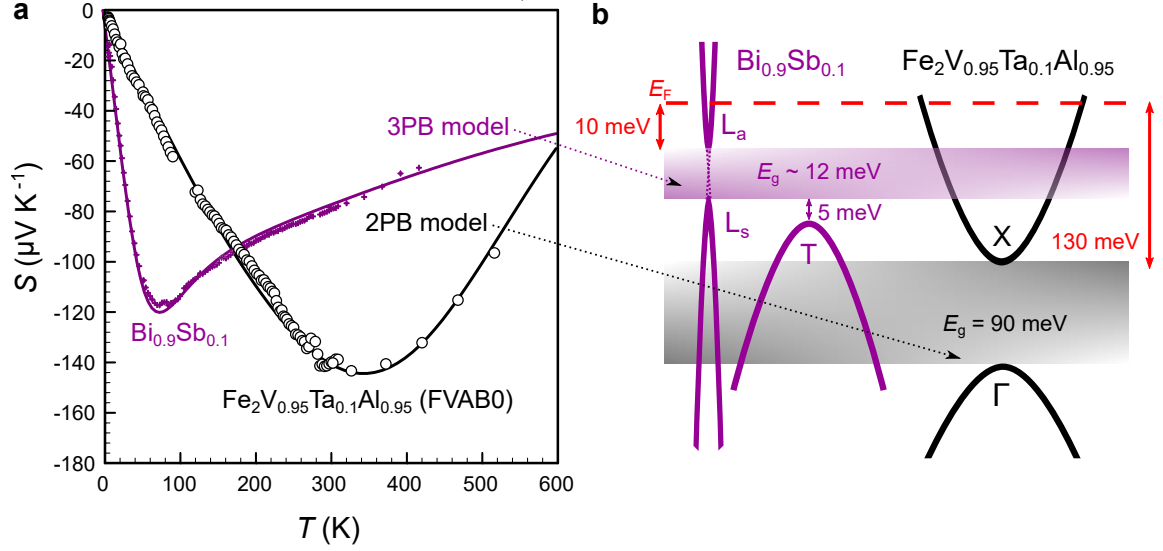


Fig. S15 | Three- and two-parabolic band modelling of the temperature-dependent Seebeck coefficient **a**, Temperature-dependent Seebeck coefficient of Heusler-type $\text{Fe}_2\text{V}_{0.95}\text{Ta}_{0.1}\text{Al}_{0.95}$ (FVAB0) and $\text{Bi}_{0.9}\text{Sb}_{0.1}$. Solid lines are least-squares fits employing a two- and three-parabolic band model, respectively. **a**, Sketch of the electronic band structure obtained from fitting $S(T)$. Energy gaps are displayed in milli electron volts and the position of the Fermi energy with respect to the band edges is displayed as a dashed red line.

8.16. Effective medium theory predictions of dimensionless figure of merit

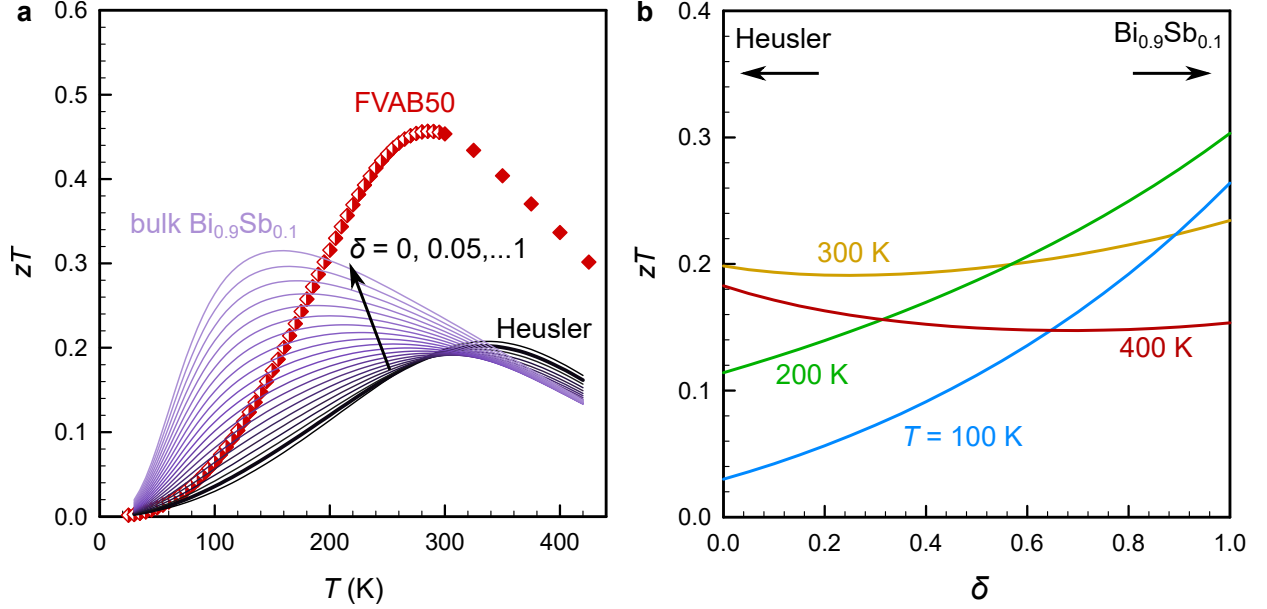


Fig. S16 | Volume fraction dependence of zT in effective medium theory. **a**, Temperature- and **b**, volume fraction-dependent zT of an effective medium comprising $\text{Bi}_{0.9}\text{Sb}_{0.1}$ in $\text{Fe}_2\text{V}_{0.95}\text{Ta}_{0.1}\text{Al}_{0.95}$ in a *parallel slabs* geometry (different geometries, e.g. random distribution, were calculated and yielded only minor differences for experimentally observed $\delta \approx 0.06$). In the framework of effective medium (EM) theory, the maximum figure of merit at any given temperature cannot exceed the maximum figure of merit of either component at the same temperature, irrespective of the geometry of the separate phases. Experimental data of the FVAB50 composite studied in this work, however, reveal a strong enhancement over EM theory, emphasizing a beneficial interplay between the two phases in the composite and/or a beneficial modification of the thermoelectric properties of the individual components.

8.17. Additional magneto-transport data of FVAB50

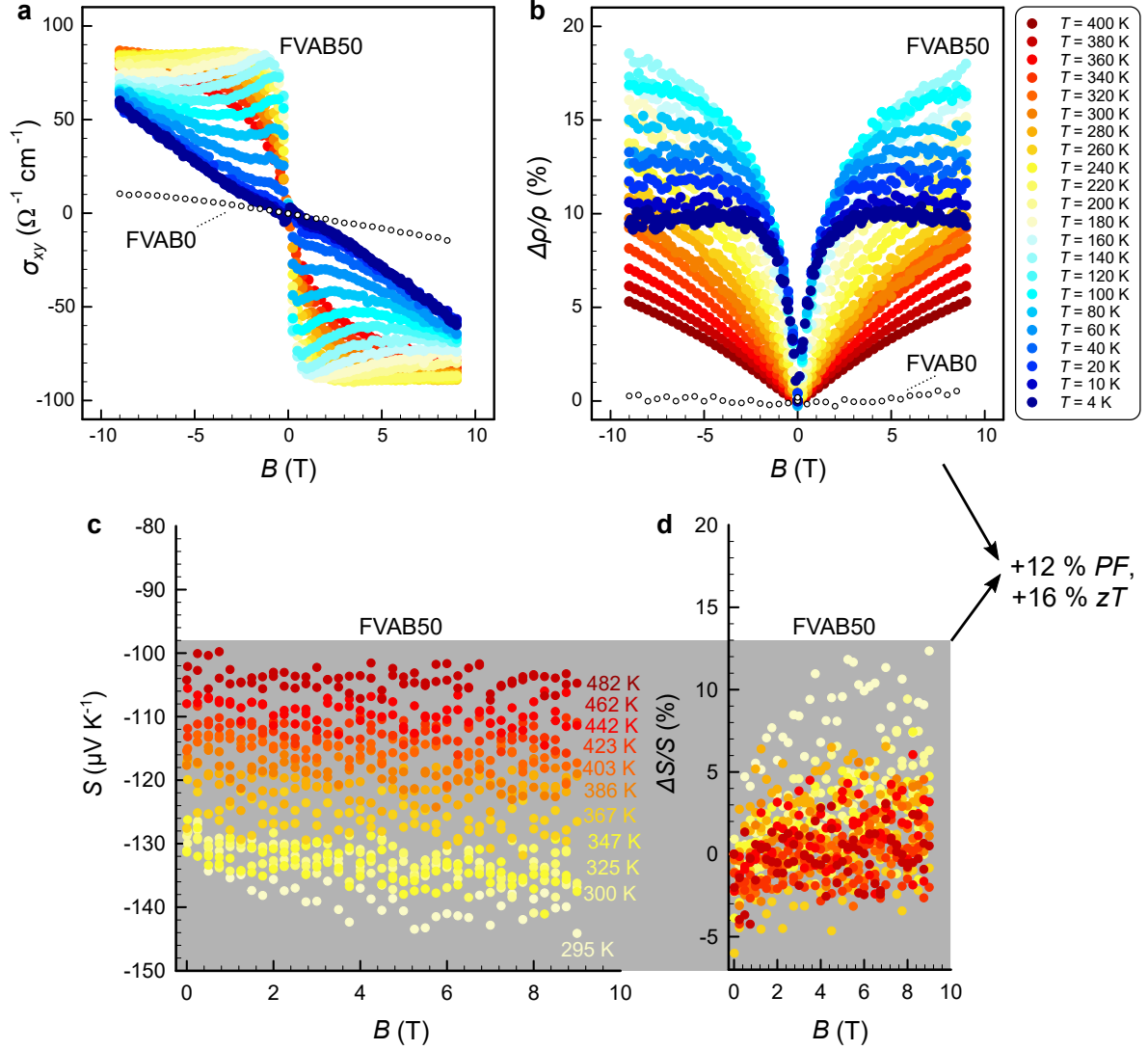


Fig. S17 | Additional field-dependent magneto-transport studies of FVAB50. **a**, Field-dependent, isothermal Hall conductivity $\sigma_{xy} = \rho_{xy}/(\rho_{xy}^2 + \rho_{xx}^2)$ and **b**, transverse magneto-resistance of FVAB50 from 2 to 400 K. Data for FVAB0 at 300 K are also shown for comparison. **c,d**, Field-dependent magneto-Seebeck effect of FVAB50 composite from 295 to 482 K.

8.18. Anomalous Hall effect of non-magnetic FVAB50 compared to other magnetic materials

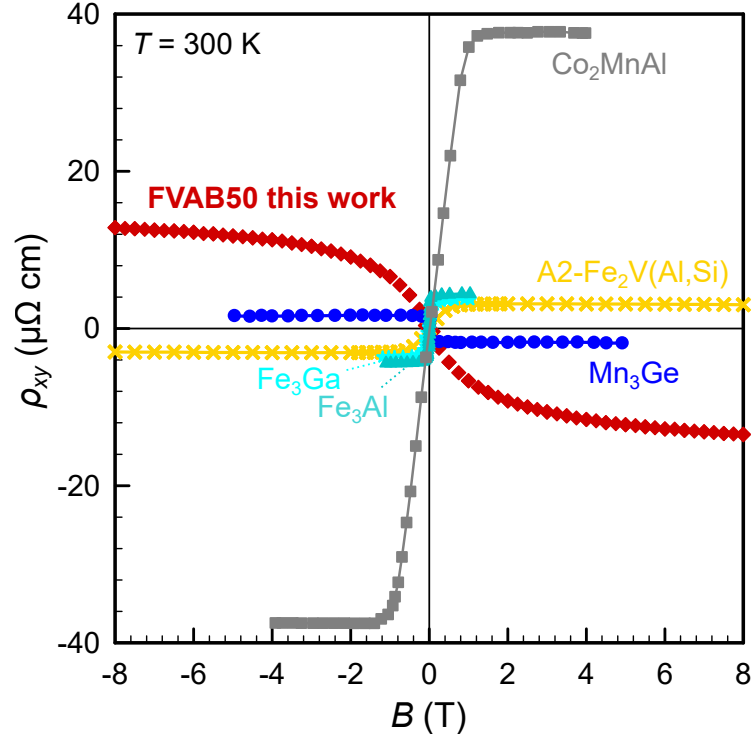


Fig. S18 | Comparison of anomalous Hall effect. Room-temperature anomalous Hall resistivity of nonmagnetic FVAB50 composite compared to other famous magnetic compounds with high anomalous Hall resistivities. The anomalous Hall effect in the former is attributed to a two-carrier channel transport of less mobile Heusler bulk carriers and Dirac-like surface electrons associated with the topological-insulating $\text{Bi}_{1-x}\text{Sb}_x$ secondary phase.

8.19. Consistency check of temperature-dependent electrical resistivity

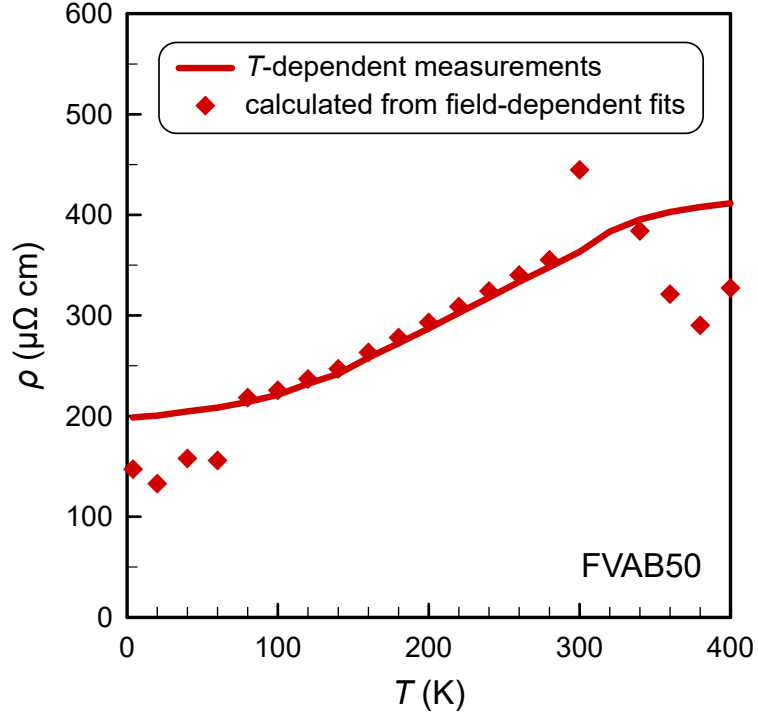


Fig. S19 | Robustness test of field-dependent Hall effect analysis. Temperature-dependent electrical resistivity of FVAB50 composite obtained directly from temperature-dependent measurements of $\rho_{xx}(T)$ and by recalculating $\rho_{xx}(T)$ from the Hall carrier mobilities and carrier concentrations derived from fitting $\rho_{xy}(B)$. The very good agreement between the two different methods highlights the robustness of the field-dependent Hall resistivity fits.

8.20. Phonon dispersion and density of states mismatch

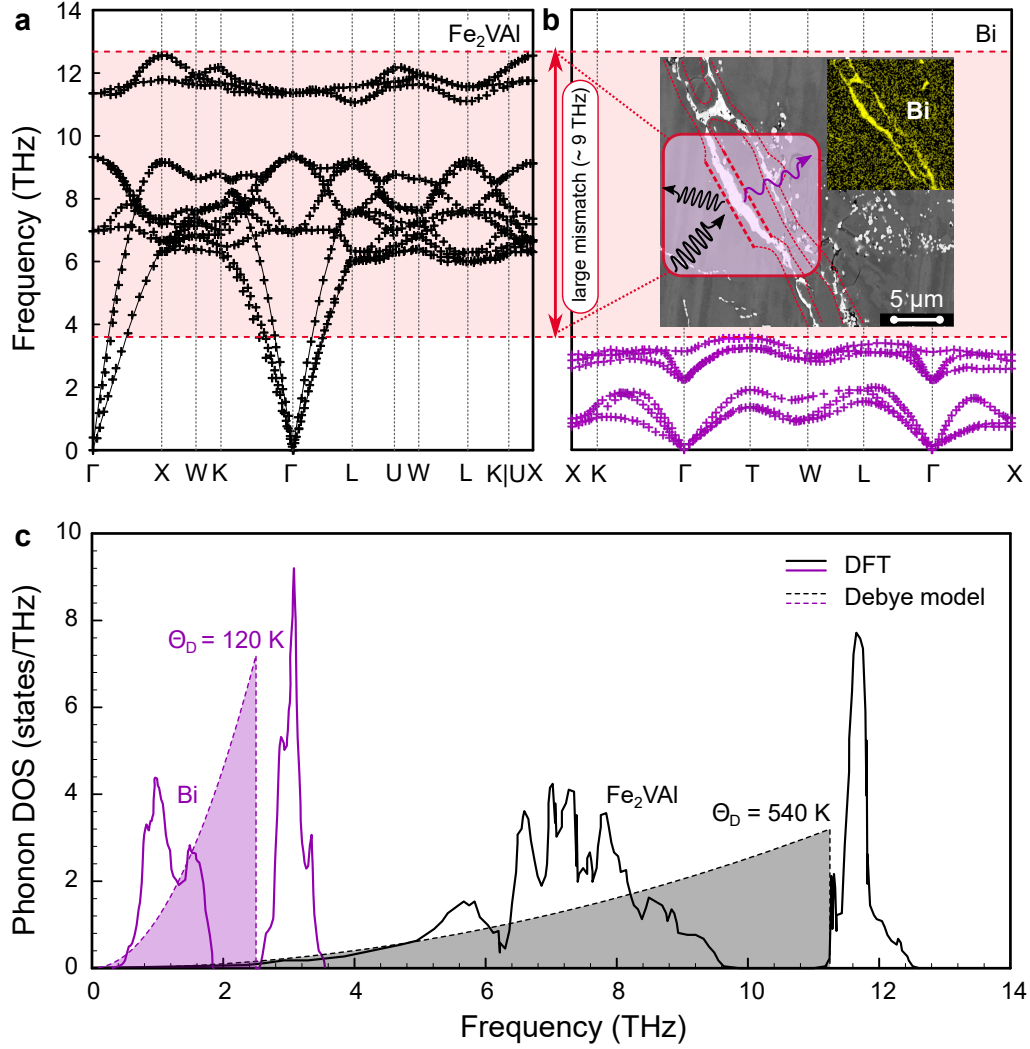


Fig. S20 | Phonon dispersions and densities of states. **a,b,** Comparison of the phonon band structure of Fe_2VAI and elemental Bi. The large mismatch of about 9 THz in the phonon dispersion implies a strong phonon energy filtering effect (see inset). **c,** Phonon densities of states from density functional theory (DFT) and in the simple Debye model approximation. The large difference in the phonon spectra is reflected also in a substantial difference of the Debye temperatures.

8.21. Comparison of thermal conductivity in different directions of the sample

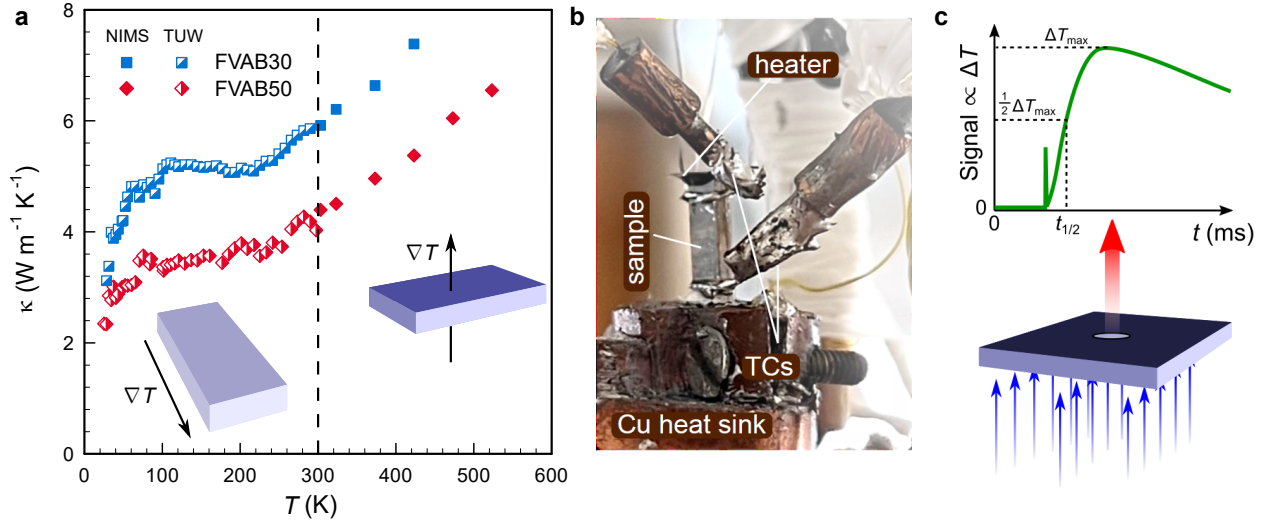


Fig. S21 | Isotropy of thermal transport in $(\text{Fe}_2\text{V}_{0.95}\text{Ta}_{0.1}\text{Al}_{0.95}+\text{Bi}_{0.9}\text{Sb}_{0.1})$ composites. **a**, Excellent agreement between low- and high-temperature measurements of the thermal conductivity rule out any anisotropy in the transport properties of the FVAB composite samples studied in this work. Low-temperature measurements were performed in the longitudinal direction, perpendicular to the compaction direction, using a steady-state method (**b**) employed in a home-built setup at TU Wien. High-temperature measurements were performed parallel to the compaction direction (see sketch in **c**), using a laser-flash method for the diffusivity and a differential scanning calorimeter for the specific heat, in a commercial setup (LFA 467, NETZSCH) at NIMS.

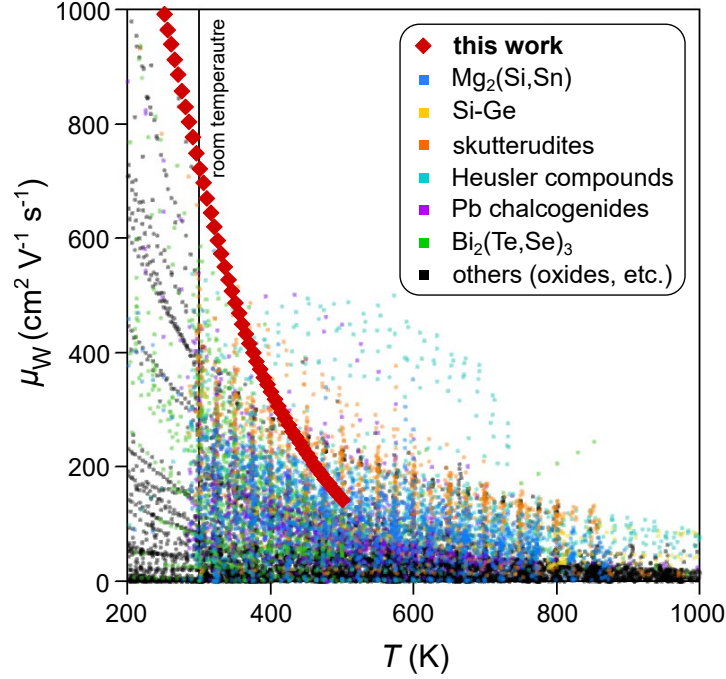


Fig. S22 | Comparison of weighted mobilities. Temperature-dependent weighted mobility of $\text{Fe}_2\text{V}_{0.95}\text{Ta}_{0.1}\text{Al}_{0.95}$ composite with 50 vol.% $\text{Bi}_{0.9}\text{Sb}_{0.1}$ added before sintering (FVAB50) compared to all other n -type thermoelectric semiconductors reported (as of July 2024) in the *Starrydata2* open web database²⁶.

References

- [1] R. Resel, E. Gratz, A. Burkov, T. Nakama, M. Higa, and K. Yagasaki, *Review of Scientific Instruments* **67**, 1970 (1996).
- [2] E. Putley, *Journal of Physics C: Solid State Physics* **8**, 1837 (1975).
- [3] A. F. May and G. J. Snyder, *Materials, preparation, and characterization in thermoelectrics*, 1 (2012).
- [4] M. Parzer, A. Riss, F. Garmroudi, J. de Boor, T. Mori, and E. Bauer, *arXiv preprint arXiv:2409.06261* (2024).
- [5] N. W. Ashcroft and N. D. Mermin, (1976).
- [6] G. Eguchi and S. Paschen, *Physical Review B* **99**, 165128 (2019).
- [7] S. Masuda, K. Tsuchiya, J. Qiang, H. Miyazaki, and Y. Nishino, *Journal of Applied Physics* **124**, 035106 (2018).
- [8] G. Rogl, D. Setman, E. Schafler, J. Horky, M. Kerber, M. Zehetbauer, M. Falmbigl, P. Rogl, E. Royanian, and E. Bauer, *Acta materialia* **60**, 2146 (2012).
- [9] G. Rogl, S. Ghosh, O. Renk, K. Yubuta, A. Grytsiv, E. Schafler, M. Zehetbauer, R. C. Mallik, E. Bauer, and P. Rogl, *Journal of Alloys and Compounds* **855**, 157409 (2021).
- [10] G. Rogl and P. F. Rogl, *Zeitschrift für anorganische und allgemeine Chemie* **648**, e202200044 (2022).
- [11] G. Rogl, M. J. Zehetbauer, and P. F. Rogl, *Materials Transactions* **60**, 2071 (2019).
- [12] G. Rogl, S. Ghosh, L. Wang, J. Bursik, A. Grytsiv, M. Kerber, E. Bauer, R. C. Mallik, X.-Q. Chen, M. Zehetbauer, *et al.*, *Acta Materialia* **183**, 285 (2020).
- [13] K. Fukuta, K. Tsuchiya, H. Miyazaki, and Y. Nishino, *Applied Physics A* **128**, 184 (2022).
- [14] F. Garmroudi, A. Riss, M. Parzer, N. Reumann, H. Müller, E. Bauer, S. Khmelevskyi, R. Podlucky, T. Mori, K. Tobita, *et al.*, *Physical Review B* **103**, 085202 (2021).

- [15] B. Hinterleitner, P. Fuchs, J. Rehak, F. Garmroudi, M. Parzer, M. Waas, R. Svagera, S. Steiner, M. Kishimoto, R. Moser, *et al.*, Physical Review B **102**, 075117 (2020).
- [16] S. Singh, I. Valencia-Jaime, O. Pavlic, and A. H. Romero, Physical Review B **97**, 054108 (2018).
- [17] Y. Kawaharada, K. Kurosaki, and S. Yamanaka, Journal of alloys and compounds **349**, 37 (2003).
- [18] M. Li, D. L. Cortie, J. Liu, D. Yu, S. M. K. N. Islam, L. Zhao, D. R. Mitchell, R. A. Mole, M. B. Cortie, S. Dou, *et al.*, Nano Energy **53**, 993 (2018).
- [19] C. Kim and D. H. Lopez, Applied Physics Letters **120** (2022).
- [20] A. Kumar and K. T. Wojciechowski, Journal of the European Ceramic Society **42**, 4227 (2022).
- [21] A. Kumar, P. Bhumla, A. Kosonowski, K. Wolski, S. Zapotoczny, S. Bhattacharya, and K. T. Wojciechowski, ACS Applied Materials & Interfaces **14**, 44527 (2022).
- [22] Z. Liang, C. Xu, H. Shang, M. Ning, T. Tong, S. Song, W. Ren, X. Shi, X. Liu, F. Ding, *et al.*, Advanced Energy Materials **13**, 2301107 (2023).
- [23] S. I. Kim, K. H. Lee, H. A. Mun, H. S. Kim, S. W. Hwang, J. W. Roh, D. J. Yang, W. H. Shin, X. S. Li, Y. H. Lee, *et al.*, Science **348**, 109 (2015).
- [24] R. Deng, X. Su, Z. Zheng, W. Liu, Y. Yan, Q. Zhang, V. P. Dravid, C. Uher, M. G. Kanatzidis, and X. Tang, Science Advances **4**, eaar5606 (2018).
- [25] J. Heremans, The Ohio State University **AFRL-AFOSR-VA-TR-2017-0084**.
- [26] Y. Katsura, M. Kumagai, T. Kodani, M. Kaneshige, Y. Ando, S. Gunji, Y. Imai, H. Ouchi, K. Tobita, K. Kimura, *et al.*, Science and Technology of Advanced Materials **20**, 511 (2019)